AGU PUBLICATIONS

JGR

Journal of Geophysical Research: Oceans

RESEARCH ARTICLE

10.1002/2014JC010396

Stratified turbulence in the nearshore coastal ocean: Dynamics and evolution in the presence of internal bores

Ryan K. Walter[1,2], Michael E. Squibb[2], C. Brock Woodson[3], Jeffrey R. Koseff[2], and Stephen G. Monismith[2]

[1]Physics Department, California Polytechnic State University, San Luis Obispo, California, USA, [2]Bob and Norma Street Environmental Fluid Mechanics Laboratory, Department of Civil and Environmental Engineering, Stanford University, Stanford, California, USA, [3]COBIA Lab, College of Engineering, University of Georgia, Athens, Georgia, USA

Key Points:
- Field measurements of stratified turbulence from turbulence flux tower
- Internal bores drive substantial changes to local turbulence and mixing
- Mixing efficiency shows power law dependence on turbulence activity number

Correspondence to:
R. K. Walter,
rkwalter@calpoly.edu

Citation:
Walter, R. K., M. E. Squibb, C. B. Woodson, J. R. Koseff, and S. G. Monismith (2014), Stratified turbulence in the nearshore coastal ocean: Dynamics and evolution in the presence of internal bores, *J. Geophys. Res. Oceans*, *119*, doi:10.1002/2014JC010396.

Received 19 AUG 2014
Accepted 24 NOV 2014
Accepted article online 27 NOV 2014

Abstract High-frequency measurements of stratified turbulence throughout the water column were collected over a 2 week period in the nearshore environment of southern Monterey Bay, CA, using a cabled observatory system and an underwater turbulence flux tower. The tower contained a vertical array of acoustic Doppler velocimeters and fast-response conductivity-temperature sensors, providing a nearly continuous data set of turbulent velocity and density fluctuations and a unique look into the stratified turbulence field. The evolution of various turbulence quantities and direct measurements of the vertical turbulent diffusivity is examined in the presence of nearshore internal bores, both in the near-bed region and in the stratified interior. We show that individual bores can drive substantial changes in local turbulence and mixing dynamics, with considerable differences between the leading and trailing edges of the bores. Using direct observations of the flux Richardson number, our measurements confirm previous observations that show the highest mixing efficiencies (Γ) occurring in regions of buoyancy-controlled turbulence. Parameterizations of the flux Richardson number as a function of the turbulence activity number are also presented. Finally, we demonstrate that the commonly used assumption of a constant mixing efficiency ($\Gamma = 0.2$) for calculating turbulent diffusivities leads to significant overestimates compared to diffusivity values calculated using the directly measured mixing efficiency. Implications of the results are discussed.

1. Introduction

Continental shelves are thought to be an important, yet highly variable, contributor to mixing and the dissipation of turbulent kinetic energy in the oceans [*Munk and Wunsch*, 1998; *Carter et al.*, 2005]. Furthermore, estimates of turbulent mixing in coastal zones are important for understanding the vertical mixing of tracers, with significant biological and ecological implications [e.g., *Boehm et al.*, 2002; *Leichter et al.*, 1996; *Pineda*, 1994]. Specifically, diapycnal mixing affects many ecologically important processes such as nutrient cycling, primary production, hypoxia development, and the mixing of tracers such as pollutants from sewage outfalls [e.g., *Wolanski and Pickard*, 1983; *Leichter et al.*, 1996; *Boehm et al.*, 2002; *Chan et al.*, 2008]. The dynamics of stratified turbulence have been investigated widely in both the laboratory [cf. *Itsweire et al.*, 1986; *Ivey and Imberger*, 1991] and numerical simulations [cf. *Holt et al.*, 1992; *Shih et al.*, 2005]; however, extensive time series measurements of stratified turbulence on the shelf are somewhat limited [see *Davis and Monismith*, 2011, and the references therein]. While microstructure profiler measurements have provided significant insight into oceanic turbulence, turbulence on the shelf is highly intermittent in time and extremely patchy in space [e.g., *Moum and Rippeth*, 2009]. Indeed, the combined effects of boundary layers (bottom and surface), variable stratification, vertical velocity shear, internal waves, and a host of other physical processes in the coastal environment contribute to the complex spatiotemporal variability of turbulence, making it difficult to obtain comprehensive measurements using discrete profiles. Turbulence measurements have expanded to moored platforms in recent years in order to capture extended time series of high-frequency events and provide a closer examination of turbulence in highly dynamic systems [cf. *Shaw et al.*, 2001; *Davis and Monismith*, 2011; *Bluteau et al.*, 2013].

In order to represent the energetics of turbulent velocity fluctuations, and also provide a means for evaluating and understanding turbulence measurements, the turbulent kinetic energy (TKE) equation is employed [e.g., *Tennekes and Lumley*, 1972]:

$$-\frac{\partial}{\partial t}\left(\frac{\overline{u_i' u_i'}}{2}\right)-U_j\frac{\partial}{\partial x_j}\left(\frac{\overline{u_i' u_i'}}{2}\right)-\frac{\partial}{\partial x_j}\left(\frac{1}{\rho_o}\overline{p' u_j'}+\frac{1}{2}\overline{u_i' u_i' u_j'}-2\nu\overline{u_i' e_{ij}}\right)-\overline{u_i' u_j'}\frac{\partial U_i}{\partial x_j}=\frac{g}{\rho_o}\overline{\rho' u_3'}+\varepsilon. \quad (1)$$

Here $x_j = [x, y, z]$ is the spatial coordinate with z positive upward, $u_i = [u, v, w]$ represents the velocity vector, $U_i = [U, V, W]$ is the time-averaged velocity vector, $u'_i = [u', v', w']$ is the turbulent velocity vector, $\rho = \rho_o + \rho'$ is the density field with contributions from time-averaged and fluctuating components, p is the pressure, ν is the kinematic viscosity, $e_{ij} = \frac{1}{2}\left(\frac{\partial u'_i}{\partial x_j} + \frac{\partial u'_j}{\partial x_i}\right)$ is the fluctuating strain rate tensor, ε is the TKE dissipation rate, and an overbar represents an appropriate Reynolds average. The first two terms on the left-hand side (LHS) represent the time rate of change of TKE and rate of change of TKE due to advection by the mean flow, respectively. The next term on the LHS represents energy flux divergences, and specifically spatial transport due to pressure fluctuations, the turbulence itself, and viscous stresses, respectively. The final term on the LHS is the shear production (P) of TKE from the mean flow through the interaction of the Reynolds stress with the mean velocity shear field. The first term on the right-hand side (RHS) denotes the buoyancy flux (B). A positive B signifies an irreversible loss of TKE to potential energy in a stably stratified fluid, while a negative B implies buoyant production of TKE (i.e., counter-gradient flux) and typically occurs in an unstably stratified fluid. The last term on the RHS represents the loss, or dissipation (ε), of TKE to internal energy by viscosity and small-scale strains.

Despite its importance for understanding turbulence measurements, there exists a paucity of the literature examining the TKE budget in marine bottom boundary layers. The assumption of equilibrium turbulence, whereby the shear production of TKE balances the dissipation of TKE ($P = \varepsilon$), has been tested in several strong tidal flows. *Gross and Nowell* [1983], *Trowbridge et al*. [1999], and *Sanford and Lien* [1999] all found that close to the bed, there was a local balance of production and dissipation. However, *Sanford and Lien* [1999] found that away from the bed, dissipation exceeded production. Likewise, *Walter et al*. [2011] surmised that the advection of nonlocal TKE was likely responsible for dissipation exceeding production near the bed in a shallow tidal flow, possibly due to inhomogeneous bathymetry and bottom roughness (i.e., vegetation). While valuable, the above studies were limited to measurements near the bed in strong tidal flows with little, or no, density stratification present.

Shaw et al. [2001] examined the TKE budget on the continental shelf in a stratified environment and found that near the bed buoyancy fluxes were negligible so that there was a local balance between production and dissipation. Further up in the water column (4.35 m above the bottom in ~70 m of water), stratification and buoyancy fluxes were important; however, the local TKE budget (i.e., $P = B + \varepsilon$) did not close. *Feddersen et al*. [2007] collected nearshore measurements close to the surf zone (~3.2 m depth) and found that shear production was much less than dissipation, concluding that nonlocal transport of turbulence was important. *Reidenbach et al*. [2006] found a local balance of production and dissipation over a coral reef and sandy bottoms near the bed (1 m above the bottom); however, these measurements were limited to the bottom mixed layer and were likely not influenced by stratification and other processes further up in the water column (water depths of 8–24 m at different sites). *Davis and Monismith* [2011] studied internal waves shoaling on the inner shelf (19 m depth) using high-frequency turbulence measurements near the bed (3 m above the bed maximum instrument height). TKE balances in this complex stratified shear-flow environment revealed that dissipation greatly exceeded production by nearly an order of magnitude, while buoyancy fluxes were generally negligible. The authors suggested that the horizontal transport of nonlocal TKE by internal wave-driven flows was responsible for the imbalance. Most recently, *Bluteau et al*. [2013] examined turbulence at several vertical locations within 30 m of the bed at a deep (~400 m) shelf site. The authors used TKE dissipation rate estimates to infer the thermal variance dissipation rate and used scaling arguments to conclude that the shear production of temperature variance was balanced by the dissipation of thermal variance. However, the TKE and thermal variance production terms were not measured so the assumed balanced could not be tested.

The aforementioned studies offer a glimpse into the knowledge gap that exists in analyzing and understanding the TKE budget in the stratified coastal environment. In particular, previous studies have been limited to near-bed measurements (i.e., within a few meters of the bed or instrument heights above the bed less than ~15% of the total water depth). Indeed, the standard conceptual model of a bottom mixed layer (i.e., vertical variations in density are much smaller than the variations across the layer boundary) under a

stratified interior is that the presence of stratification acts to dampen vertical velocity fluctuations and limits vertical penetration of the bottom-generated TKE. However, recent observations of nearshore internal bores reveal that the dissipation of turbulent kinetic energy in the stratified interior, estimated using isopycnal slope spectra, is comparable, and in some cases, greater than the dissipation of TKE associated with bottom-generated turbulence [*Walter et al*., 2012]. Additionally, there have been an increased number of observations documenting the generation of TKE by nonlinear internal waves in the stratified interior [e.g., *Moum et al*., 2003; *Woodson et al*., 2011]. It is clear that the turbulence structure in the presence of nonlinear internal waves and bores may be substantially different than that expected from the standard model of a bottom mixed layer under a stratified interior. Questions arise as to how the TKE budget will evolve throughout the water column in the presence of stratified shear flows such as those seen with nonlinear internal waves and bores, and in particular the importance of the first three terms on the LHS of equation (1), with important implications for vertical mixing processes.

This study looks at high-frequency turbulence measurements throughout the water column in the nearshore coastal environment, both in the stratified interior and near the bed. We take advantage of a cabled observatory system at Hopkins Marine Station of Stanford University in southern Monterey Bay, CA, which allows for nearly continuous measurements in time. Nearshore internal bores are a common feature that produce transient stratification and mixing events, and represent the dominant source of variability, in this ecologically important region [*Walter et al*., 2012] (see *Walter et al*. [2014] for a description of how regional-scale upwelling and changing offshore (shelf) conditions influence the observed bores). Internal bores at this site are marked by an upslope surging flow of subthermocline water that tends to stratify the water column (leading edge of the bore, or the "bore period" from *Walter et al*. [2012]). This period is followed by a strongly sheared downslope flow in the form of a warm-front, high-frequency temperature oscillations, and elevated levels of turbulent dissipation, as the bore features relax back downslope (trailing edge of the bore, or the "mixing period" from *Walter et al*. [2012]). However, it is important to note that the isopycnal slope spectra method used to calculate turbulent dissipation was only appropriate during the "mixing period," and the TKE dissipation represented a time-averaged value over the mixing period (∼several hours) [see *Walter et al*., 2012]. A more detailed examination of how the nearshore internal bores affect TKE dissipation, as well as other turbulence quantities, across the various periods, or phases, of the bores is warranted.

The main objective of this work is to better characterize the dynamics of stratified turbulence in the nearshore coastal environment. We also seek to better understand the evolution of turbulence in the presence of nearshore internal bores. Not only do these measurements provide a better understanding of the modification to the turbulence dynamics by internal bores, but they also comprise one of the most comprehensive sets of stratified turbulence data collected in the coastal environment. In section 2, we introduce the field site, the experimental setup and underwater turbulence flux tower, and data processing methods. Section 3 describes the evolution of the turbulence dynamics at various heights throughout the water column, including the strongly stratified interior, during various conditions and in the presence of nonlinear internal bores. Section 4 highlights and describes the various stratified turbulence regimes observed, as well as turbulent mixing dynamics. Finally, we summarize the findings and discuss implications in section 5.

2. Site Description, Experimental Setup, and Methods

2.1. Site Description and Experimental Setup

Monterey Bay is located along the central coast of California within the highly productive California Current Large Marine Ecosystem (CCLME) (Figure 1a). It is a semienclosed embayment that features one of the largest submarine canyons on the west coast of the United States. Monterey Bay also contains a narrow continental shelf with about 80% of the bay shallower than 100 m [*Breaker and Broenkow*, 1994]. Additionally, it is home to large commercial fisheries, as well as some of the west coast's largest kelp (*Macrocystis pyrifera*) forests, the latter of which are a critical habitat and nursery for nearshore biological communities.

Tides in Monterey Bay are mixed semidiurnal, with currents dominated by the M_2 (∼12.42 h period) tidal component [cf. *Rosenfeld et al*., 2009; *Carter*, 2010]. Moreover, large amplitude internal waves are a well-documented feature along the continental margin in and around Monterey Submarine Canyon, where isopycnal displacements can reach hundreds of meters [e.g., *Breaker and Broenkow*, 1994; *Petruncio et al*., 1998; *Kunze et al*., 2002]. The current study was conducted in southern Monterey Bay at Hopkins Marine Station of

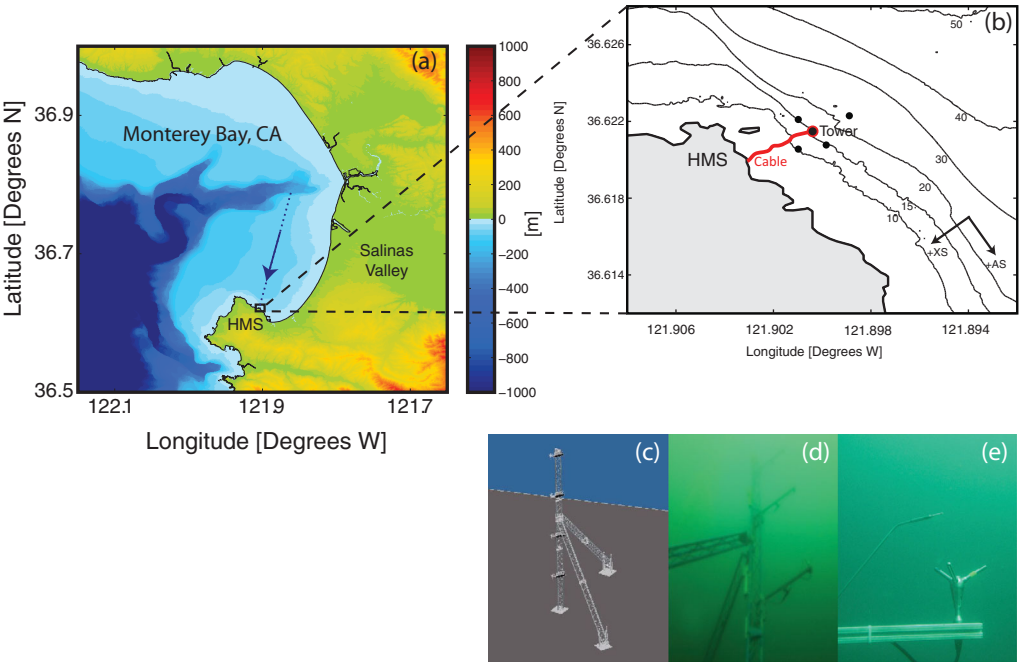

Figure 1. (a) Bathymetry and topography of the Monterey Bay, CA, region with the study site indicated by a black box. Also shown is the median bore propagation heading from *Walter et al*. [2012] (blue arrow). (b) Study site with the moorings shown as filled black circles, as well as the location of the turbulence flux tower (black circle with red outline) and the approximate location of the cabled observatory system (cable—red line). Bathymetry contours (10, 15, 20, 30, 40, 50 m isobaths) are also shown along with the location of Hopkins Marine Station (HMS—Stanford University). (c) Computer animated drawing of the turbulence flux tower (M. Squibb). (d) Turbulence flux tower deployed in the field, showing the arms with ADV/fast CT combos (shown are the 4, 6, and 8 mab arms). (e) Example ADV and colocated fast CT deployed in the field.

Stanford University (HMS—Figure 1), the location of previous observations of nearshore internal bores [*Walter et al*., 2012, 2014]. This study utilizes a cabled observatory system at HMS, the Kelp Forest Array (KFA) [*Walter*, 2014, Appendix B]. The KFA is composed of a cable from shore that contains fiber optic cables for Ethernet and copper wires carrying 300 VDC. This cable connects to an underwater "node" located several hundred meters offshore near the 15 m isobath (Figure 1b). This underwater "node" distributes 24/48 VDC and Ethernet to various "subnodes," which are used to interface with oceanographic instruments. The subnodes also power the instruments and convert data streams from serial to Ethernet. Data are then acquired using virtual serial ports on a remote computer on shore.

The current study was part of a larger project (Monterey Tower Node—MOTOWN) aimed at understanding how nearshore internal bores affect circulation dynamics and turbulent mixing in the nearshore coastal environment. Here, we focus on the stratified turbulence dynamics, as well as the evolution of the turbulence in the presence of nearshore internal bores. Various budgets (e.g., energy, momentum, etc.), will be investigated in future contributions. As such, only the relevant instrumentation and data used in this study will be described in detail [cf. *Walter*, 2014, Appendix B].

The centerpiece of this experiment was an 8 m tall underwater turbulence flux tower that was deployed near the 15 m isobath next to the underwater subnodes (Figures 1b–1e). On the submerged tower, we attached six Nortek acoustic Doppler velocimeters (ADVs) at 0.3, 1, 2, 4, 6, and 8 m above the bed (mab) fixed to arms that protruded approximately 1 m away from the tower (Figures 1c–1e). The ADVs were leveled by divers to within 1° using a bubble level, and the arms were positioned so that they were extending out from the tower (60° from true north). Each of the ADVs was equipped and synched with a Precision Measurement Engineering, Inc. (PME) fast-response thermistor (FP07) and conductivity (ceramic plate) sensor (fast CT). The fast CTs were positioned to sample approximately 1 cm away from the ADV sampling volume [i.e., $<10l_k$, where l_k is the Kolmogorov length scale defined by equation (16)] so that colocated measurements of velocity (ADVs) and density (fast CTs) were obtained. All of the ADV/fast CT combos were synched together to ensure a common time base and then connected to the KFA cabled observatory

system. This allowed continuous, colocated measurements of turbulent velocity and density fluctuations at 64 Hz for nearly 2 weeks (14:00 on 8 August 2012 to 08:00 on 21 August 2012). This configuration also enabled us to measure turbulent fluxes of momentum and density.

Surrounding the tower, we deployed an array of densely instrumented moorings that collected velocity and temperature (density) measurements throughout the water column (Figure 1b). Findings from these surrounding moorings will be discussed in a future contribution, and hence the detailed mooring configurations are not included here. In addition to the ADV/fast CT vertical array, the tower was also equipped with 22 SBE56 temperature loggers throughout the water column [0–9 m above the bed (mab) in 0.5 m increments, 10, 11, 12 mab], all of which sampled at 0.5 s periods [see *Walter et al*., 2014]. There was also a SBE39 temperature logger at the surface location, sampling at 10 s intervals. In addition, the tower included SBE37 conductivity-temperature-depth (CTD) loggers at 0 (24 s), 2 (6 s), 4 (6 s), 6 (6 s), and 8 (24 s) mab, where the sampling period is denoted in parentheses for each vertical location. In order to measure vertical profiles of velocity throughout the water column, a RDI 1200 kHz Workhorse acoustic Doppler current profiler (ADCP) was deployed at the tower location. The ADCP sampled in fast-ping Mode 12 (six subpings per 1 s ensemble) with 0.5 m vertical bin spacing. This sampling scheme results in a small error standard deviation of 0.12 cm/s for 10 min averages. The ADCP was also leveled by divers to within 1° of the horizontal using a bubble level in order to minimize instrument tilt errors.

2.2. Methods

2.2.1. Data Processing

Velocity measurements from the ADCP and ADVs were rotated into cross-shore (u), alongshore (v), and vertical velocity (w) components using the principal axes obtained from a long-term ADCP near the site (Figure 1b). The principal axes of the long-term record were within 2° of those calculated from the ADCP in the current study. During the summer upwelling season in Monterey Bay, salinity variations are sufficiently small such that density is mainly controlled by temperature [e.g., *Woodson et al*., 2009, 2011; *Walter et al*., 2012, 2014]. Analysis of the tower CTD data showed that small changes in salinity varied linearly with temperature throughout the water column (e.g., $R^2 = 0.91$, p value < 0.001 for the 2 mab CTD) with nearly identical linear regression coefficients between different depths. Consequently, densities were calculated at all tower thermistor locations using the observed temperature and derived linear relationship from the CTD measurements for salinity as a function of temperature. All times referenced in the text and figures are in local time, Pacific Daylight Time, unless otherwise noted.

Spectral and coherence calculations were performed using the fast Fourier transform (FFT), using standard methods [e.g., *Walter et al*., 2011]. Hamming windows with 50% overlap between adjacent segments were used. The window length, and hence the number of windows in each 10 min segment, was chosen by taking into account the number of degrees of freedom (DOF) for confidence intervals, frequency resolution, and length of the original record. A chi-square variable analysis and the equivalent number of DOF (EDOF) were used to calculate confidence intervals for the spectra. For the coherence analysis, confidence limits were quantified using the EDOF [*Emery and Thomson*, 2004].

2.2.2. Turbulence Analysis and Quantities

For the turbulence analysis, ADV and fast CT data were processed using 10 min intervals with 50% overlap. This standard averaging interval represents a trade-off between capturing an appropriate number of realizations of the desired turbulent length scales and maintaining quasi-stationary statistics [e.g., *Soulsby*, 1980; *Davis and Monismith*, 2011; *Walter et al*., 2011]. Quality control (QC) of the ADV and fast CT data was performed by removing ADV data points with correlations less than 70% and temporal derivatives (i.e., accelerations) greater than the acceleration due to gravity. Following this, the phase-space threshold filtering method of *Goring and Nikora* [2002], which utilizes first-order and second-order differencing and a Universal criterion, was used to identify data spikes. When ADV velocity data points were removed based on the above criterion, the corresponding fast CT data points were also removed so that buoyancy flux calculations would not be biased. Following removal, individual erroneous data spikes were replaced using a linear interpolation between neighboring points. Longer sections of bad data were replaced with white noise scaled by the velocity variance in the particular 10 min segment. The scaled white noise contained a flat spectral signature and did not affect statistics and turbulence quantities. Ten minute segments with more than 15%

removed data were not used for further analysis. These initial QC criteria resulted in ~39.8% of the 10 min segments being rejected.

Another important consideration for the data quality control is wake effects from the tower and supporting legs. Analysis of velocity spectrograms [*Walter*, 2014, Appendix B] reveals varying degrees of wake interference for velocities with mean horizontal directions oriented such that the velocity vector passes through the tower and legs (i.e., 30°–90° from true north). Hence, 10 min segments with this mean directionality (~8.3% of QC data) were removed from further analysis.

In order to accurately calculate various turbulence statistics and quantities, such as momentum/buoyancy fluxes and dissipation, it is necessary to account for the effects of surface waves (i.e., wave-turbulence decomposition). Previous studies [e.g., *Shaw et al*., 2001; *Davis and Monismith*, 2011, see reference below] have successfully removed surface wave contamination of the turbulence signal by using a differencing method between vertically separated sensors, which was originally developed by *Trowbridge* [1998], and later updated by *Shaw and Trowbridge* [2001] and *Feddersen and Williams* [2007] to include adaptive filtering. Briefly, this method assumes that turbulence is uncorrelated between adjacent sensors, or that the vertical separation between sensors is greater than the largest turbulent length scale, so that motions that are correlated between the sensors are due to waves. Thus, by differencing the two velocity signals, only the turbulence component remains. Unfortunately, the adaptive filtering method was not successful in separating waves and turbulence in the current data set based on inspection of the velocity spectra and cospectra in the wave band frequencies (not shown). This technique also proved unsuccessful in the surface layer observations of *Gerbi et al*. [2008], and the near-bed observations of *MacVean and Lacy* [2014]; the authors attributed the failure of the differencing method to multidirectional waves and decorrelated motions at higher frequencies, respectively. Analysis of velocity spectrograms [*Walter*, 2014, Appendix B] in the current study reveals that sensors at different heights measured wave energy at different frequencies. For instance, while increased energy was often seen in the lower frequencies associated with longer period surface waves (~10 s periods) at most vertical locations, the shorter period waves were mainly seen in the spectra of the upper tower instruments. Various differencing combinations of the vertical locations were explored unsuccessfully.

Thus, to separate waves and turbulence, we employ the spectral "phase" decomposition method of *Bricker and Monismith* [2007]. This method has been successfully used in previous field studies in a variety of coastal and estuarine locations [e.g., *Hansen and Reidenbach*, 2012; *Wilson et al*., 2013; *MacVean and Lacy*, 2014]. Briefly, this method utilizes the phase lag between the velocity components (e.g., u and w) of surface waves to interpolate the magnitude of the turbulence under the wave peak. When considering the two-sided cross-spectral density (CSD) of u and w, the turbulence spectrum can be expressed as the difference between the spectrum of raw velocities and that of the wave-induced velocities. Integrating under the spectrum of each component, leads to an expression for the turbulent Reynolds stress,

$$\overline{u'w'} = \overline{uw} - \overline{\tilde{u}\tilde{w}}, \tag{2}$$

where primes and tildes denote fluctuating and wave components, respectively.

By writing the Fourier coefficients (U_j, W_j) in phasor notation (e.g., $U_j = |U_j| e^{i\angle U_j}$, where $\angle U_j$ is the phase) and utilizing the Euler relation, the wave stress (i.e., last term in equation (2)) can be determined from the data series by summing over the two-sided spectral domain, where the odd (imaginary) component gives no contribution:

$$\overline{\tilde{u}\tilde{w}} = \sum_{j=wave-peak} |\tilde{U}_j||\tilde{W}_j| \cos\left(\angle W_j - \angle U_j\right), \tag{3}$$

here the magnitude of $\tilde{U}_j$ ($\tilde{W}_j$) is the difference between the raw U_j (W_j) and the turbulence U_j' (W_j'), which is found by interpolating the autospectral density (PSD) of u (w) below the wave peak using a least squares fit to the data to the left and right of the identified wave band (e.g., Figure 2b). The turbulent Reynolds stress is then found by subtracting the wave stress, which is found by integrating the wave component of the CSD over the wave peak (equation (3)), from the integral of the total stress over the full frequency domain using equation (2). We refer the reader to *Bricker and Monismith* [2007] for further details.

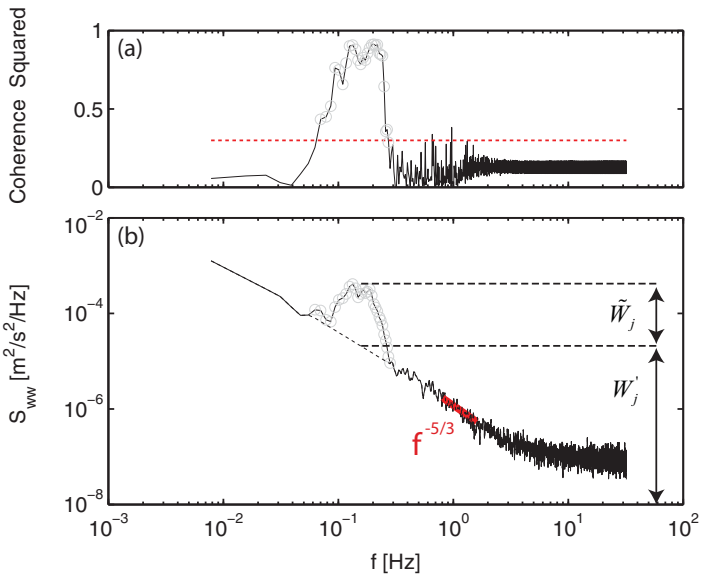

Figure 2. Example wave-turbulence decomposition for a representative 10 min data series at the 4 mab ADV. (a) Coherence squared between the vertical velocity component and the pressure signal (solid black line). Gray dots denote the identified wave band, or the frequency components that are significantly coherent (i.e., above the 95% confidence level denoted by the dashed red line) in the wave band. (b) Power spectral density (PSD) of the vertical velocity component (S_{ww}—solid black line). Gray dots denote the data points within the wave band, and the dashed black line is a least squares fit to the data to the left and right of the wave band (see section 2). The wave component ($\tilde{W}_j$) is found by subtracting the PSD above the dashed black line in the wave band region. Also shown is −5/3 power law fit in the inertial subrange (solid red line).

The aforementioned approach relies on an accurate delineation of the frequency range of the waves for interpolation of the PSD. For each 10 min segment, we calculated the coherence between the vertical velocity component and the ADV pressure signal and identified the wave band by those frequency components that showed a statistically significant coherence within the frequency range 0.05–0.4 Hz, which encompasses the range of wave frequencies observed in the spectra over the experiment (e.g., Figure 2a). Upon inspection of the velocity spectra and cospectra, this method proved robust in accurately capturing the wave band (e.g., Figure 2b). Moreover, the cumulative integral of the wave-filtered cospectra (Ogive curves) resembled the expected forms, at least to the degree generally reported in the literature [cf. *Kaimal et al.*, 1972; *Walter et al.*, 2011; *Walter*, 2014, Appendix B]. The same methodology was employed to calculate the alongshore component of the Reynolds stress ($\overline{v'w'}$), turbulent density fluxes ($\overline{\rho'w'}$), and each TKE component $\left[k=\frac{1}{2}\left(\overline{u'u'}+\overline{v'v'}+\overline{w'w'}\right)\right]$.

Using a data set from a similar turbulence tower setup at the Kilo Nalu Observatory in Mamala Bay, HI, where the *Feddersen and Williams* [2007] differencing method proved successful, the *Bricker and Monismith* [2007] performed equally well in the wave-turbulence decomposition and calculation of momentum and density fluxes (M. E. Squibb et al., personal communication, 2014). Finally, in order to limit the effects of unsteady advection of turbulence by the waves, we restricted further analysis to periods when $\sigma_{U_h}/U_h < 2$ (∼10.2% of QC data); σ_{U_h} is an estimate of the surface wave orbital velocities, and is calculated as the standard deviation of the horizontal velocity components in each 10 min window (i.e., $u_h=\sqrt{u^2+v^2}$), while U_h is the mean horizontal flow speed. This limitation is comparable to that used in similar studies of turbulence estimates in the presence of surface wave forcing [e.g., *Gerbi et al.*, 2008; *Davis and Monismith*, 2011].

Using the wave-removed momentum fluxes, the shear production (P) of TKE was calculated from equation (1) as,

$$P=-\overline{u'w'}\frac{\partial U}{\partial z}-\overline{v'w'}\frac{\partial V}{\partial z}, \tag{4}$$

where the vertical gradients of the mean horizontal velocities (U and V) were calculated from the ADVs. Similar shear production results were achieved using the velocity gradients estimated from the ADCP at the tower, as well as various spline fits to the ADV and ADCP velocity data. The buoyancy flux (B) term in the TKE equation (equation (1)) was calculated using the wave-removed density flux,

$$B=\frac{g}{\rho_o}\overline{\rho'w'}. \tag{5}$$

Dissipation of TKE was estimated using Kolmogorov's −5/3 law and an inertial subrange fit following the method outlined in *Feddersen et al.* [2007]. This method uses the high-frequency portion of the vertical velocity spectrum together with the *Lumley and Terray* [1983] model for the effect of the surface waves on

the turbulent wave number spectrum to calculate dissipation, since waves act to advect turbulent eddies past the instrument sensor and alias wave energy into higher frequencies than the wave band frequencies. Dissipation was calculated at various radian frequencies (ω),

$$\varepsilon(\omega) = \left[\frac{S_{w'w'}(\omega)2(2\pi)^{3/2}}{\alpha M_{w'w'}(\omega)}\right]^{3/2}, \tag{6}$$

where $\alpha = 1.5$ is Kolmogorov's constant, $S_{w'w'}$ is the vertical velocity spectrum, and $M_{w'w'}$ is an integral over three-dimensional wave number space that depends on the wave-orbital velocities and mean flow [*Lumley and Terray*, 1983; *Feddersen et al*., 2007]. The spectrum of vertical velocities was used since this velocity component is the least noisy [e.g., *Voulgaris and Trowbridge*, 1998].

Dissipation was calculated at various cyclic frequencies (0.8, 1.0, 1.2, 1.4, and 1.6 Hz) within the inertial subrange. This particular range of frequencies encompasses a region that is higher than the dominant wave band, lower than the noise floor, and consistently produced a $-5/3$ power law fit (e.g., Figure 2). Dissipation estimates at the various cyclic frequencies produced consistent results, indicating that the *Lumley and Terray* [1983] model for the wave advection of frozen turbulence is reasonable [cf. *Feddersen et al*., 2007]. Following *Feddersen et al*. [2007], a frequency-averaged dissipation value (hereafter referred to as ε) is obtained for every 10 min segment using a log-mean of the dissipation values at the various cyclic frequencies.

Furthermore, we restricted the dissipation estimates to 10 min segments that satisfied the condition, $\frac{u'_{h,rms}}{U_h} < 0.3$ ($\sim$9.2% of QC data), where $u'_{h,rms}$ is the root-mean-square of the turbulent velocity fluctuations along the mean horizontal flow direction. This criterion ensures that Taylor's frozen turbulence hypothesis, which is used to convert measurements from frequency to wave number space, is valid [see *Bluteau et al*., 2011, and the references therein]. Additionally, dissipation estimates that did not yield a $-5/3$ power law fit in the inertial subrange were rejected ($\sim$16.5% of QC data). This was implemented by computing the least squares power law fit to the spectra in the inertial subrange and discarding estimates in each 10 min window where the coefficient of regression (R^2) between the power law fit and the *Feddersen et al*. [2007] fit (i.e., $-5/3$ power law) was less than 0.7 [cf. *Bluteau et al*., 2011]. This particular cutoff effectively eliminated periods where a $-5/3$ fit was not achieved, ensuring the existence of an inertial subrange. As discussed later in the manuscript, turbulence activity numbers, $\varepsilon/\nu N^2$, where $N^2 = -\frac{g}{\rho_o}\frac{\partial \overline{\rho}}{\partial z}$ is the buoyancy frequency squared and is a measure of the strength of stratification, were generally well above 100, further ensuring a well-defined inertial subrange with minimal anisotropic effects [see *Gargett et al*., 1984; *Bluteau et al*., 2011, and the references therein]. Uncertainty in the dissipation estimates was quantified by calculating dissipation with equation (6) using the upper and lower confidence intervals (90%) of the vertical velocity spectra, and the method outlined above. The minimum (maximum) uncertainty bound on the dissipation estimates was a decrease (increase) by a factor of 0.49 (1.49), which does not significantly alter any of the results or conclusions.

The traditional approach of estimating the vertical turbulent diffusivity of density (κ_ρ) is to utilize the *Osborn* [1980] steady state formulation,

$$\kappa_\rho = \Gamma \frac{\varepsilon}{N^2}, \tag{7}$$

where Γ is the mixing coefficient. The mixing coefficient (Γ) is related to the flux Richardson number (R_f) [e.g., *Ivey and Imberger*, 1991],

$$R_f = \frac{B}{B+\varepsilon}, \tag{8}$$

by the following relation,

$$\Gamma = \frac{R_f}{1-R_f}. \tag{9}$$

In equation (1), the RHS represents TKE sink terms; TKE is transferred to internal energy through viscous dissipation at a rate ε, and in a stably stratified fluid, to potential energy through the buoyancy flux. Thus, the flux Richardson number, which is related to the mixing coefficient by equation (9), represents the ratio of

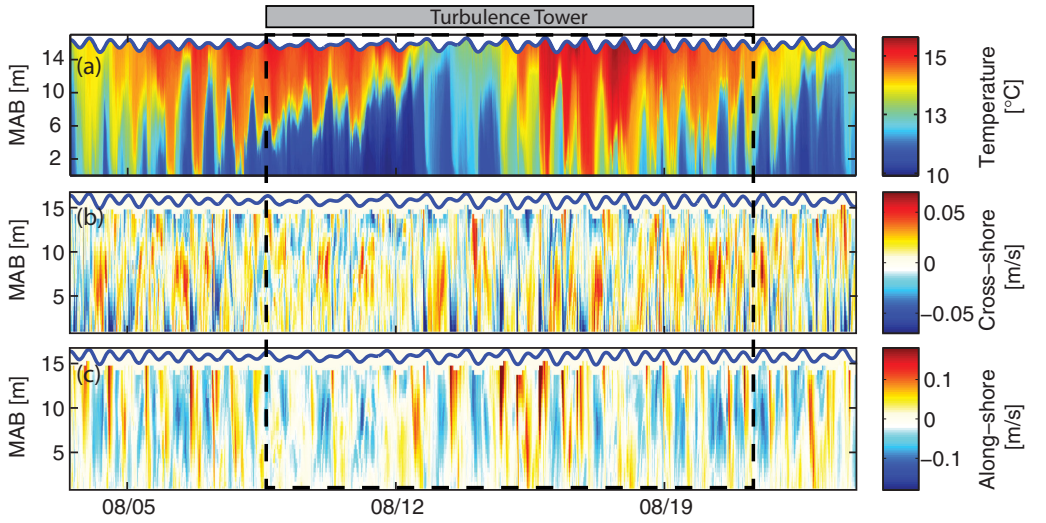

Figure 3. Time series over the entire study period at the tower location of the (a) vertical temperature structure, (b) vertical structure of the cross-shore velocity field (10 min averages, positive onshore), and (c) vertical structure of the alongshore velocity field (10 min averages, positive into the bay). The location of the sea surface (blue line) is also shown in Figures 3a–3c. The dashed black box indicates the time period during which the underwater turbulence tower collected measurements.

the amount of TKE lost to potential energy for a stably stratified fluid to the net mechanical energy available to sustain turbulent motions (i.e., LHS of equation (1), which is equal to $B + \varepsilon$) [cf. *Ivey and Imberger*, 1991; *Davis and Monismith*, 2011; *Dunckley et al*., 2012]. Whereas the conventional approach is to estimate κ_ρ using a constant mixing coefficient, $\Gamma = 0.2$ ($R_f = 0.17$), in equation (7), here we are able to directly calculate the mixing coefficient using equations (8) and (9), and hence the vertical diffusivity,

$$\kappa_\rho = \frac{R_f}{1-R_f}\frac{\varepsilon}{N^2}. \tag{10}$$

Clearly from the definition in equation (8), equation (10) for calculating κ_ρ is identical to, $\kappa_\rho = \frac{B}{N^2}$, obtained from the eddy diffusivity model formulation [cf. *Osborn*, 1980],

$$-\overline{\rho' w'} = \kappa_\rho \frac{\partial \bar{\rho}}{\partial z}. \tag{11}$$

3. Results

3.1. General Observations

We summarize briefly here the mean temperature and velocity dynamics during the experiment to provide a basis for the interpretation of the turbulence measurements, which is the focus and new contribution of this manuscript. For a more detailed examination of the mean dynamics during the experiment, we refer the reader to *Walter et al*. [2014]. The detailed temperature structure over the entire study period reveals episodic cold water intrusions that propagate in (onshore/upslope flow) and out (offshore/downslope flow) of the nearshore (Figure 3). These intrusions are typical of nearshore internal bores that act to drive transient stratification and mixing events [e.g., *Walter et al*., 2012]. The record is also characterized by several distinct regimes that change the nearshore temperature structure and stratification. From approximately 7 to 14 August and starting again on about 21 August, the nearshore is marked by a low-frequency "pooling" of cold water throughout the bottom portions of the water column (Figure 3a). This increases the stratification in the nearshore, causing the bores to perturb the preexisting thermocline. This is in contrast to periods where the nearshore is well mixed (i.e., uniform temperature throughout the water column). In this case, the bores propagate into the well-mixed waters and act to stratify the water column.

Walter et al. [2014] show that the two nearshore regimes are related to the regional wind-driven upwelling cycles and offshore stratification. During weak upwelling conditions, the offshore thermocline is deeper,

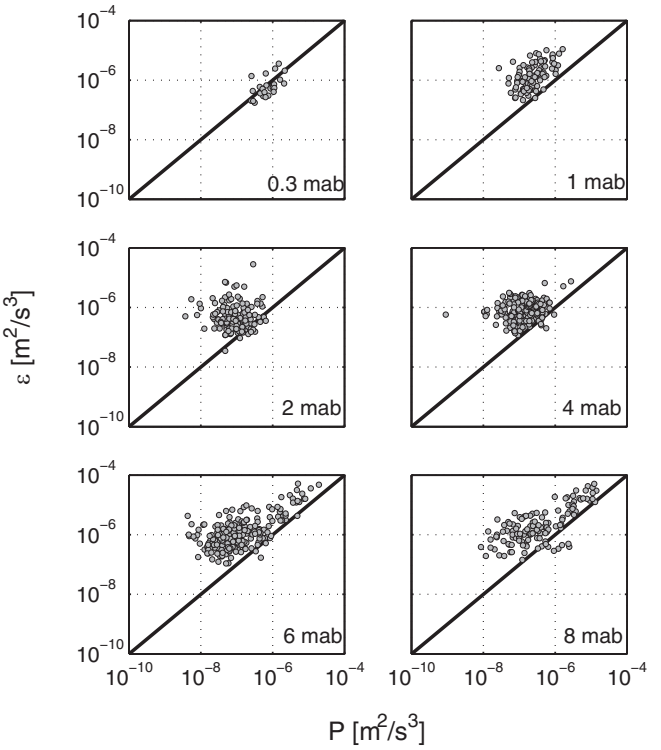

Figure 4. Dissipation (ε) versus shear production (P) of TKE at various heights above the bed. Individual events are indicated with gray circles, while the solid black line represents equilibrium turbulence ($P = \varepsilon$).

and the nearshore internal bores propagate into well-mixed waters. During upwelling-favorable conditions, the offshore thermocline shoals toward the surface, nearshore "pooling" develops as subthermocline waters inundate the nearshore, and nearshore internal bores perturb the preexisting stratification. Noteworthy is the fact that the bores stratify the water column at higher frequencies (approximately semidiurnal period) than the upwelling cycles (~7–10 day period) that drive the nearshore pooling, and they also drive the major perturbations to the preexisting stratification.

Examination of the velocity structure reveals that the bore events contribute to the majority of the variance in the cross-shelf velocity field. This is confirmed using an empirical orthogonal function (EOF) analysis [see *Walter et al.*, 2014]. We refer the reader to *Walter et al.* [2012, 2014] for a more detailed examination of the cross-shore and alongshore velocity and shear fields in the presence of the nearshore internal bores.

3.2. TKE Budget

Figure 4, which shows a scatterplot of ε versus P at the various instrument heights, highlights the relative magnitude of these two terms at these various elevations. Clearly, classical boundary layer equilibrium turbulence, whereby shear production of TKE is locally balanced by the dissipation of TKE (i.e., $P = \varepsilon$), does not hold everywhere throughout the water column. As will be discussed later, this is probably due to the presence of stratification and nonlinear internal bores. Near the bed (0.3 mab), the production balances dissipation and the assumption of equilibrium turbulence appears valid. This is consistent with previous observations of near-bed turbulence in strong tidal flows and coastal environments [*Gross and Nowell*, 1983; *Trowbridge et al.*, 1999; *Sanford and Lien*, 1999; *Shaw et al.*, 2001; *Reidenbach et al.*, 2006]. However, Figure 4 also reveals that further away from the bed, the local balance begins to break down.

Specifically, the dissipation of TKE is much greater than the local shear production of TKE, by roughly an order of magnitude. Including the buoyancy flux term (B), as well as the TKE vertical transport term [i.e., $\frac{\partial}{\partial z}\left(\overline{kw'}\right)$] from equation (1), does not improve the imbalance; these terms are typically one to several orders of magnitude smaller than the shear production and dissipation terms, consistent with previous studies [e.g., *Shaw et al.*, 2001; *Davis and Monismith*, 2011]. Such nonequilibrium turbulence ($P \neq \varepsilon$), especially away from the bed, has been previously observed in strong tidal flows [*Sanford and Lien*, 1999; *Walter et al.*, 2011], as well as coastal environments [*Shaw et al.*, 2001; *Feddersen et al.*, 2007; *Davis and Monismith*, 2011] (M. E. Squibb et al., personal communication, 2014).

Furthermore, even when calculating the shear production using the total stress values (e.g., no wave removal, or $\overline{uw}$ and $\overline{vw}$), dissipation is still greater than production. We note that the comparison of production versus dissipation appears to be independent of the strength of surface wave forcing (i.e., σ_{U_h}/U_h). Also, TKE dissipation values calculated with the *Feddersen et al.* [2007] method during periods of low wave forcing ($\sigma_{U_h}/U_h \ll 1$) were similar to those obtained using an inertial subrange method that does not take

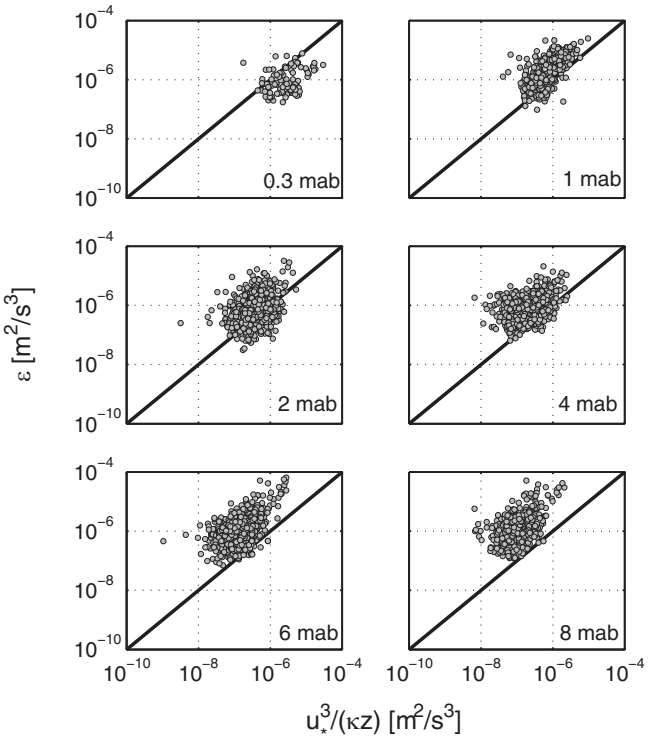

Figure 5. Observed dissipation of TKE (ε) versus the bottom boundary layer scaling (i.e., law of the wall) for dissipation, $u_*^3/\kappa z$ at various heights above the bed. The friction velocity, u_*, was estimated using the magnitude of the near-bed, horizontal Reynolds stresses at the 1 mab ADV, while the height above the bed, z, varied. Individual events are indicated with gray circles, while the solid black line represents the one-to-one relationship expected in a canonical boundary layer shear flow.

into account the effect of the waves on the high-frequency portion of the spectrum [e.g., *Shaw et al*., 2001, equation (7); *Davis and Monismith*, 2011, equation (A(1))] when comparing dissipation values above $10^{-6.5}$ m^2/s^3.

These results indicate that the contribution from the first three terms on the LHS of equation (1) cannot be neglected. We surmise that the elevated levels of dissipation are partially due to the horizontal transport of TKE, whereby turbulence is generated and advected to the measurement site where it is locally dissipated. This hypothesis seems plausible at the current study site given the energetic nonlinear internal waves that may be breaking and advecting remotely generated turbulence to the tower location [cf. *Davis and Monismith*, 2011] (*Arthur and Fringer*, personal communication, 2014). While we are not able to test this hypothesis with the available data, the examination of local turbulent dissipation and mixing by breaking internal waves (bores) at various locations along a sloping shelf is the subject of ongoing numerical work (*Arthur and Fringer*, 2014; see also *Becherer and Umlauf* [2011] and *Lorrai et al*. [2011] for a discussion on shear-induced stratification, convection, and mixing on sloping boundaries in lakes). Therefore, the assumption of equilibrium turbulence in the presence of nonlinear internal waves, especially away from the bed, is likely not appropriate in all such environments.

We also test the applicability of the classic law of the wall scaling for dissipation,

$$\varepsilon = \frac{u_*^3}{\kappa z}, \tag{12}$$

where $\kappa = 0.41$ is the Von Kármán constant, z is the height above the bed, and u_* is the friction velocity [*Pope*, 2000]. The friction velocity is estimated using the magnitude of the near-bed Reynolds stresses,

$$u_*^2 = \sqrt{\left(-\overline{u'w'}\right)^2 + \left(-\overline{v'w'}\right)^2}. \tag{13}$$

Figure 5 highlights the boundary layer scaling for dissipation at the various instrument heights. Closer to the bed (0.3, 1, and 2 mab), the law of the wall scaling for dissipation typically matches the order of magnitude of the observed dissipation values. Further up in the water column, however, the scaling begins to break down with the law of the wall scaling underpredicting the observed dissipation values. This result is expected and likely due to the presence of stratification that acts to modify the logarithmic region and the applicable turbulent length scales (i.e., the turbulent eddies outside of the constant-stress wall region no longer scale as the distance from the wall) [e.g., *Perlin et al*., 2005].

3.3. Evolution of Turbulence and Mixing in the Presence of Bores

Figure 6 highlights the density and velocity structure, turbulence shear production and dissipation, and measured vertical diffusivity over the entire record during which the turbulence tower collected

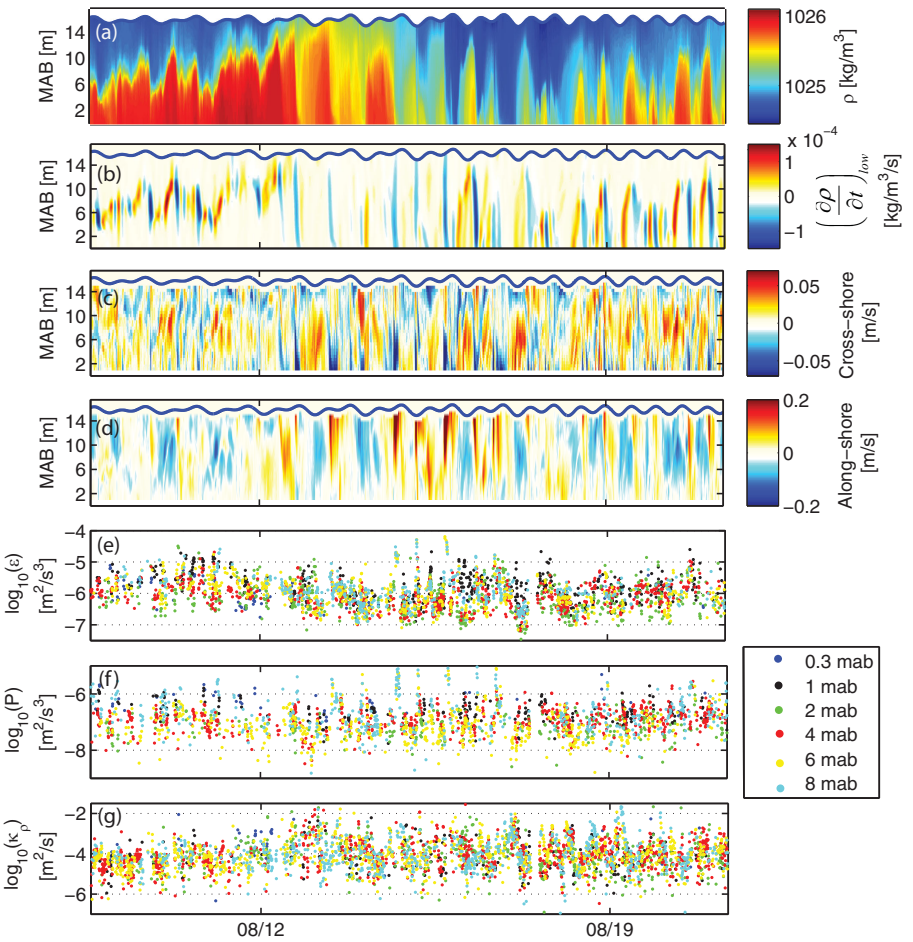

Figure 6. Time series over the entire study period at the tower location of the (a) vertical density structure, (b) low-pass filtered, time derivative of density, (c) vertical structure of the cross-shore velocity field (10 min averages, positive onshore), (d) vertical structure of the alongshore velocity field (10 min averages, positive into the bay), (e) dissipation (ε) of TKE at various heights above the bed, (f) shear production (P) of TKE at various heights above the bed, and (g) vertical turbulent diffusivity, $\kappa_\rho = \frac{B}{N^2} = \frac{R_f}{1-R_f}\frac{\varepsilon}{N^2}$, at various heights above the bed. The location of the sea surface (blue line) is also shown in Figures 6a–6d. Missing values in Figures 6e–6g correspond to periods that did not fit the quality control criteria for each respective variable (see section 2).

measurements. Also shown is the vertical structure of the time derivative of density (Figure 6b), which is meant to highlight the leading (positive derivative; "bore period" from *Walter et al.* [2012]) and trailing (negative derivative; "mixing period" from *Walter et al.* [2012]) edges of the bores. The derivative was low-pass filtered (3 h half-amplitude period) in order to better delineate the bore interface and reduce some of the higher-frequency variability. Examination of the turbulence shear production and dissipation (Figures 6e and 6f) reveals large fluctuations (changes of several orders of magnitude) that appear to be coherent with the bore events. The measured vertical diffusivity also shows large variations that are seemingly linked to the bore events, with many of the values well above the canonical value of $\sim 10^{-5}$ m^2/s for the ocean interior [*Gregg*, 1989; *Waterhouse et al.*, 2014]. We examine these trends in further detail below by first examining individual bore events in each of the two previously mentioned nearshore regimes: a well-mixed nearshore, and a stratified nearshore (nearshore "pooling").

Figure 7 highlights nearshore internal bores propagating into well-mixed waters. The arrival of the initial bore ($\sim$00:00, leading edge) is characterized by a dense mass of water that tends to stratify the water column, as well as a strong onshore (upslope) flow near the bottom in the cross-shore direction. There is a corresponding increase in the density time gradient along the bore interface, highlighted by the isopycnals in Figures 7a–7d. The arrival of the bore is also marked by a decrease in the dissipation throughout the water column, except for the near-bottom sensors (0.3 and 1 mab), which display an order of magnitude larger dissipation values compared to the stratified interior. Examination of the turbulence shear production

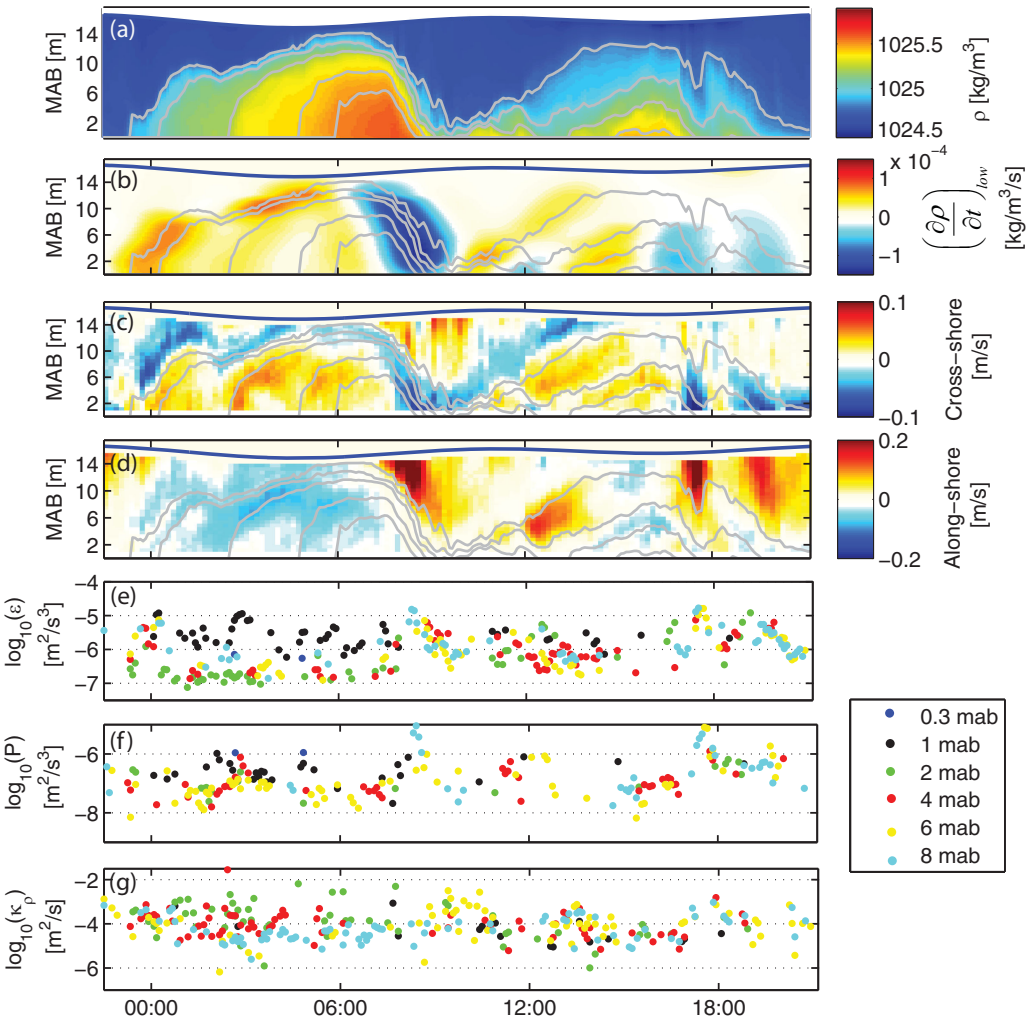

Figure 7. Example nearshore internal bore event (16 August 2012) propagating into well-mixed waters at the tower location. (a) Vertical density structure, (b) low-pass filtered, time derivative of density, (c) vertical structure of the cross-shore velocity field (10 min averages, positive onshore), (d) vertical structure of the alongshore velocity field (10 min averages, positive into the bay), (e) dissipation (ε) of TKE at various heights above the bed, (f) shear production (P) of TKE at various heights above the bed, and (g) vertical turbulent diffusivity, $\kappa_\rho = \frac{B}{N^2} = \frac{R_f}{1-R_f}\frac{\varepsilon}{N^2}$, at various heights above the bed. Isopycnals (gray lines: 1025.5, 1025.4, 1025.2, 1025.0, and 1024.8 kg/m^3), as well as the location of the sea surface (blue line), are also shown in Figures 7a–7d. Missing values in Figures 7e–7g correspond to periods that did not fit the quality control criteria for each respective variable (see section 2).

reveals slightly smaller values during the bore arrival, except for several small peaks (e.g., ~02:30) that correspond to times of elevated velocity shear. The vertical diffusivities demonstrate slightly lower values further up in the water column during the arrival of the bore.

During the relaxation of the bore (see *Walter et al*. [2012] for a discussion on the dynamics of the bore structure) in Figure 7 (~08:00, trailing edge), the water column structure quickly changes as the bore advects back offshore (downslope). There is a corresponding sharp decrease and change in sign of the density time derivative. Turbulence dissipation in the stratified interior peaks by nearly 2 orders of magnitude during the trailing edge of the bore, and is comparable to the near-bed dissipation values seen during the bore. This facet is consistent with the observations of *Walter et al*. [2012] (i.e., dissipation in the stratified interior comparable to near-bed dissipation during the "mixing period"), but the current data set provides a more complete description of the temporal and spatial evolution. There is also a sharp increase in the turbulence shear production, which is due to the large increase in shear. Careful examination reveals that the vertical diffusivity peaks slightly further up in the water column following the trailing edge of the bore. The second bore event shown in Figure 7 (~12:00 to 18:00) more clearly shows the peaks in dissipation, production, and vertical diffusivity during the trailing edge of the bore in comparison to the leading edge.

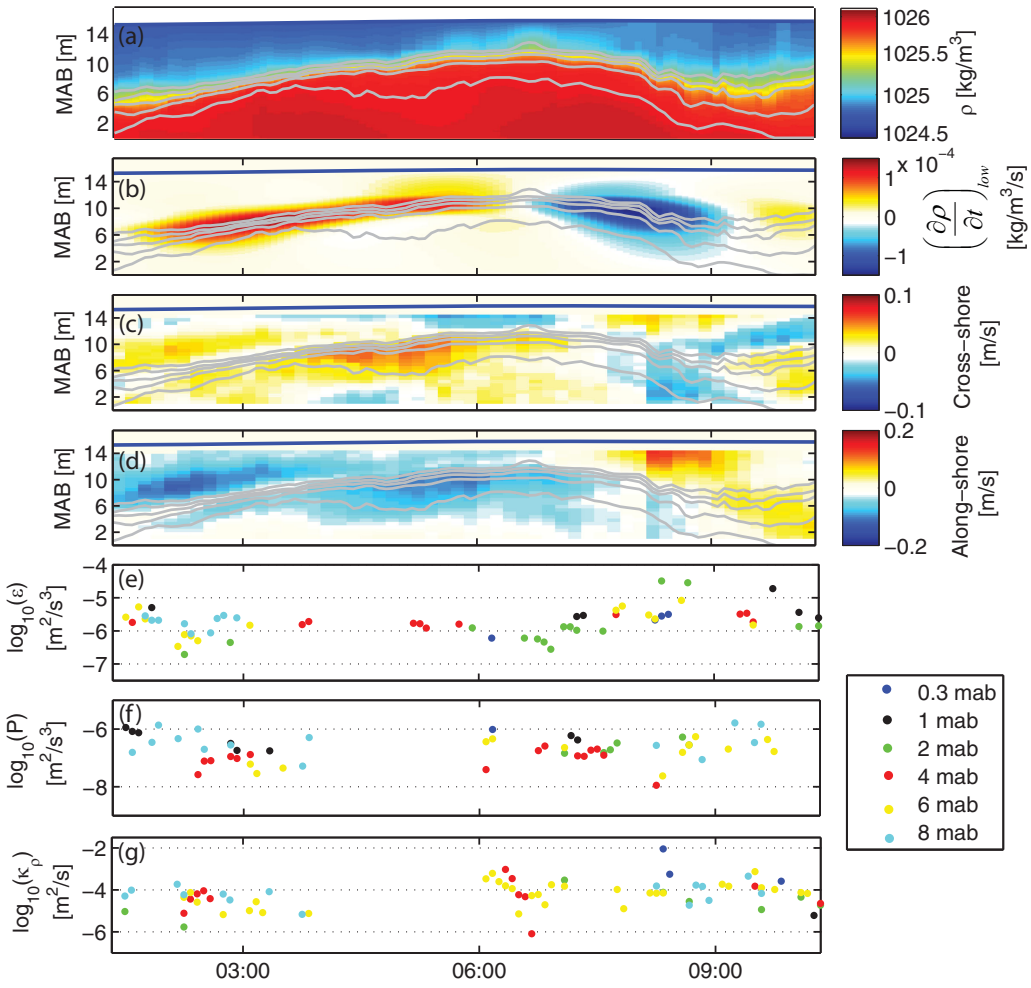

Figure 8. Example nearshore internal bore event (10 August 2012) propagating into stratified waters at the tower location. (a) Vertical density structure, (b) low-pass filtered, time derivative of density, (c) vertical structure of the cross-shore velocity field (10 min averages, positive onshore), (d) vertical structure of the alongshore velocity field (10 min averages, positive into the bay), (e) dissipation (ε) of TKE at various heights above the bed, (f) shear production (P) of TKE at various heights above the bed, and (g) vertical turbulent diffusivity, $\kappa_\rho = \frac{B}{N^2} = \frac{R_f}{1-R_f}\frac{\varepsilon}{N^2}$, at various heights above the bed. Isopycnals (gray lines: 1025.9, 1025.8, 1025.6, 1025.4, and 1025.2 kg/m^3), as well as the location of the sea surface (blue line), are also shown in Figures 8a–8d. Missing values in Figures 8e–8g correspond to periods that did not fit the quality control criteria for each respective variable (see section 2).

We also examine the detailed structure of an individual bore propagating into a preexisting stratification in Figure 8. In this case, the bore perturbs the nearshore pycnocline region, as seen in the density time gradient and cross-shelf velocity fields. While there is a large gap of discarded turbulence data from the quantity control restrictions, the turbulence structure seems to follow the same trends observed earlier. That is, the arrival of the bore coincides with decreases in the turbulence dissipation, shear production, and vertical diffusivity, while there appears to be increases in these parameters during the trailing edge.

We expand on the individual bore event findings and consider the evolution of various turbulence terms averaged across all bore events. Here, we focus on the bore interface and assess how the various phases of the bore (e.g., leading versus trailing edge) affect the stratified turbulence dynamics. The bore interface can be thought of as the nearshore pycnocline since it coincides with the region of the strongest stratification in the nearshore and separates the nearshore waters from the denser offshore waters. Figure 9 shows how various turbulence quantities, bin-averaged across all measurements at all instrument heights, vary as a function of the low-pass filtered time derivative of density. The density time derivative captures the phases of the bore (e.g., positive values, leading edge; negative values, trailing edge). Calculations were also restricted to regions of strong density stratification where $N^2 > 10^{-3.5}$ 1/s^2, which effectively isolates the bore interface.

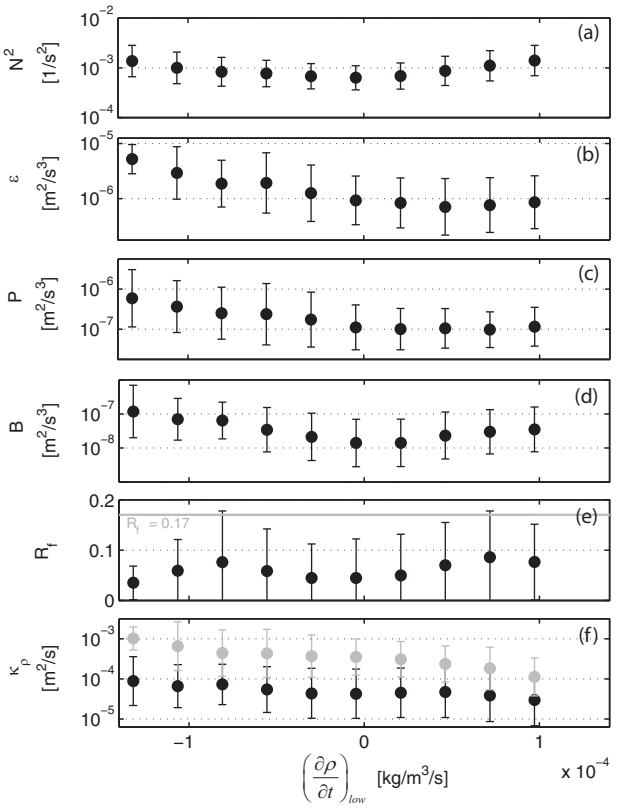

Figure 9. (a) Buoyancy frequency squared (N^2), (b) dissipation of TKE (ε), (c) shear production (P) of TKE, (d), buoyancy flux (B), (e) flux Richardson number (R_f), and (f) vertical turbulent diffusivity calculated using the measured R_f, $\kappa_\rho = \frac{B}{N^2} = \frac{R_f}{1-R_f}\frac{\varepsilon}{N^2}$ (black circles), and a constant $R_f = 0.17$ (gray line, Figure 9e), $\kappa_\rho = 0.2\frac{\varepsilon}{N^2}$ (gray circles), all as a function of the low-pass filtered, time derivative of density. Black circles represent bin-averaged values using measurements at all instrument heights, while the error bars signify the standard deviation of the bin-averaged results. Calculations were restricted to regions of strong density gradients ($N^2 > 10^{-3.5}$ 1/s^2) to isolate the bore interface (see text for details).

Figure 9a reveals that the density stratification peaks slightly in the leading and trailing edges of the bore. Furthermore, in accord with the individual bore observations presented above, the dissipation (Figure 9b) and shear production (Figure 9c) of TKE increase in the trailing edge of the bore by almost an order of magnitude compared to the other phases. In order to assess the evolution of the stratified turbulence and turbulent mixing, the buoyancy flux (Figure 9d) and the flux Richardson number (Figure 9e) were computed. As expected based on the density stratification, the buoyancy flux shows maximum values in the leading and trailing edges of the bore. On the other hand, the flux Richardson number, which is related to the mixing efficiency by equation (9), illustrates a minimum in the trailing edge of the bore, whereas the leading edge of the bore shows much larger values. Also shown is the often assumed constant value of $R_f = 0.17$, which corresponds to a constant mixing efficiency of $\Gamma = 0.2$. It is clear that the mixing efficiencies calculated along the bore interface are much smaller than this constant value, with significant variation with respect to the bore phase. While the trailing edge of the bore is more turbulent than other phases, the efficiency of mixing is smaller. This leads to measured turbulent diffusivities (Figure 9f) that are not as large as expected under the assumption of a constant mixing efficiency, but that are still slightly higher than the other phases of the bore. Indeed, employing the traditional approach of estimating turbulent diffusivity by assuming a constant mixing efficiency leads to large overestimates of the diffusivity (shown in gray in Figure 9f), particularly in the trailing edge.

4. Discussion

4.1. Stratified Turbulence Regimes and Mixing Efficiency

The nature of stratified turbulence, and the influence of buoyancy, is often evaluated in a turbulent Reynolds number (Re_t) and turbulent Froude number (Fr_t) parameter space [e.g., *Ivey and Imberger*, 1991; *Davis and Monismith*, 2011; *Dunckley et al.*, 2012]. Before defining these quantities, several important length scales are first introduced [cf. *Itsweire et al.*, 1986; *Shih et al.*, 2005]. In the absence of buoyancy effects, the Prandtl mixing-length scale characterizes the size of the energy-containing turbulent eddies,

$$l_m = \left\{ \frac{\left[\left(-\overline{u'w'} \right)^2 + \left(-\overline{v'w'} \right)^2 \right]^{1/2}}{S^2} \right\}^{1/2}, \tag{14}$$

where $S^2 = \left(\frac{\partial U}{\partial z}\right)^2 + \left(\frac{\partial V}{\partial z}\right)^2$. However, the presence of density stratification and buoyancy limits the size of the largest turbulent eddies. The Ozmidov scale represents the length scale at which buoyancy forces are equal to inertial forces, and is the largest turbulent scale allowed by buoyancy forces,

$$l_o = \left(\frac{\varepsilon}{N^3}\right)^{1/2}. \tag{15}$$

The turbulent eddies at the largest scales transfer energy through the inertial subrange to smaller and smaller scales until molecular viscosity acts to dissipate TKE into internal energy. The scale at which turbulent motions are damped by viscous forces, or the scale at which TKE is dissipated by viscosity and small-scale strains, is defined as the Kolmogorov length scale,

$$l_k = \left(\frac{\nu^3}{\varepsilon}\right)^{1/4}. \tag{16}$$

In a density stratified medium, the range of possible turbulent length scales is bounded by the Kolmogorov scale at the smallest end and the Ozmidov scale at the largest end. The turbulent overturning length scale, and the largest turbulent length scale in a statistical sense [cf. *Itsweire et al.*, 1986], is defined using the Ellison length scale,

$$l_e = \frac{\rho'_{rms}}{\partial\overline{\rho}/\partial z}. \tag{17}$$

where ρ'_{rms} denotes the root-mean-square of the turbulent density fluctuations. However, the Ellison length scale is difficult to measure in the field and is affected by internal waves [*Itsweire et al.*, 1986; *Davis and Monismith*, 2011]. DNS simulations of a stratified shear flow indicate that in the energetic regime (i.e., $\varepsilon/\nu N^2 > 100$), which is the case for nearly all measurements here, a constant relationship between the Ellison and Prandtl mixing-length scale exists ($l_e \approx 2.5 l_m$) [*Shih et al.*, 2005]. This relationship will be used for calculations of the Ellison length scale in what follows [cf. *Davis and Monismith*, 2011].

Using these length scale definitions, the turbulent Reynolds number, which is the ratio of the inertial to viscous forces in the energy-bearing eddies, is defined as follows,

$$\mathrm{Re}_t = \left(\frac{l_e}{l_k}\right)^{4/3}. \tag{18}$$

The turbulent Froude number represents the ratio of the inertial forces to the buoyant forces in the energy-bearing eddies,

$$Fr_t = \left(\frac{l_o}{l_e}\right)^{2/3}. \tag{19}$$

Figure 10 shows all of the measurements at each vertical location in the Re_t-Fr_t parameter space. The parameter space has been divided into three regions that classify the nature of the stratified turbulence: the buoyancy-affected region (Region 1), the buoyancy-controlled region (Region 2), and a region where the combination of buoyancy and viscosity completely suppress turbulent motions (Region 3) [e.g., *Luketina and Imberger*, 1987; *Ivey and Imberger*, 1991]. Measurements at the current study site are confined to Regions 1 and 2, with most of the observations occurring in the buoyancy-controlled region (Region 2, Figure 10a). Figure 10b displays the percentage of points at each vertical location in each of the three regions. The near-bed measurements (0.3 mab) are predominately in Region 1, while further up in the water column, the majority of the points lie in Region 2.

Figure 11 highlights the distribution of several parameters in the Re_t-Fr_t space. The turbulence activity number, which can also be recast in terms of the Ozmidov and Kolmogorov length scales, $\frac{\varepsilon}{\nu N^2} = \left(\frac{l_o}{l_k}\right)^{4/3}$, is shown in Figure 11a. Nearly all of the measurements fall into the energetic regime (i.e., $\varepsilon/\nu N^2 > 100$ [*Shih et al.*, 2005]), with values as large as 10^6. Examination of the flux Richardson number (Figure 11b) reveals that the largest values occur in the buoyancy-controlled region, with the majority of the observations falling below the "critical," or commonly used, value of 0.17. These results seem to suggest that the largest values of R_f do not occur near $Fr_t = 1$ [see *Ivey and Imberger*, 1991], but that the most efficient mixing occurs when the

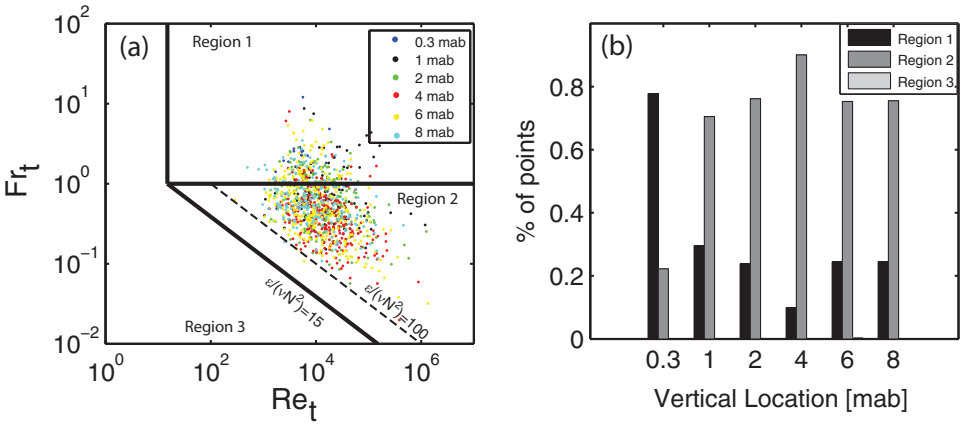

Figure 10. (a) Turbulent Froude number (Fr_t) versus turbulent Reynolds number (Re_t) diagrams for all measurements. The color circles represent measurements at the various vertical tower locations. The solid black lines denote the three regions identified by *Ivey and Imberger* [1991] (see text for details). The dashed black line indicates $\varepsilon/\nu N^2 = 100$. (b) Histogram indicating the percentage of points in each of the three regions in Figure 10a for each vertical location. Note that Region 3 was largely absent from the data set.

eddy overturning scale (l_e) is greater than the Ozmidov scale (l_o). *Davis and Monismith* [2011] (direct estimates of Γ, field measurements) and *Dunckley et al.* [2012] (parameterized estimates of Γ, field measurements) find a similar trend (i.e., maximum efficiency in Region 2), with the former noting that it is likely due to internal wave forcing and the nonlocal advection of TKE. Furthermore, the finding that the most efficient mixing occurs near $Fr_t = 1$ was based on parameterizations from laboratory results with an average Re_t of approximately 40, which is several orders of magnitude smaller than the observations here (e.g., Figures 10a and 11).

In many oceanic applications, the mixing efficiency is often taken to be a constant, $\Gamma = 0.2$; however, as discussed in recent review by *Ivey et al.* [2008], a host of laboratory experiments and DNS simulations over the

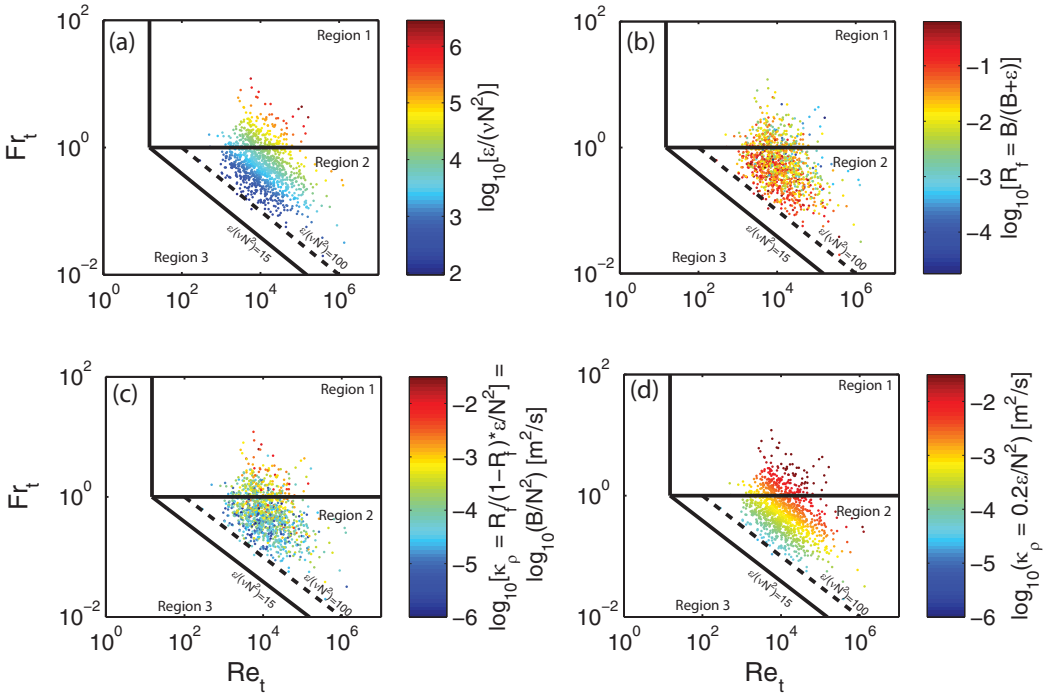

Figure 11. Turbulent Froude number (Fr_t) versus turbulent Reynolds number (Re_t) diagrams for all measurements. The color scale represents the (a) turbulence activity number ($\varepsilon/\nu N^2$), (b) the flux Richardson number (R_f), (c) the vertical turbulent diffusivity calculated using the measured R_f, $\kappa_\rho = \frac{B}{N^2} = \frac{R_f}{1-R_f}\frac{\varepsilon}{N^2}$, and (d) the vertical turbulent diffusivity calculated using a constant $R_f = 0.17$, $\kappa_\rho = 0.2\frac{\varepsilon}{N^2}$. The solid black lines denote the three regions identified by *Ivey and Imberger* [1991] (see text for details). The dashed black line indicates $\varepsilon/\nu N^2 = 100$.

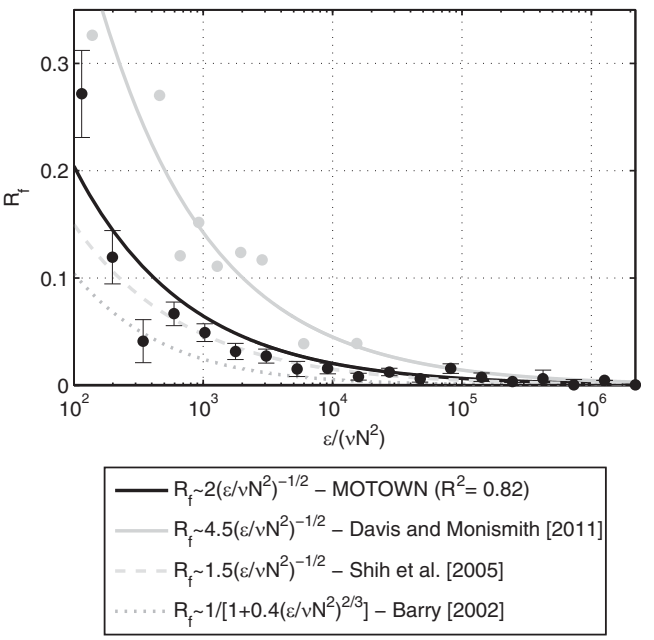

Figure 12. The flux Richardson number (R_f) as a function of the turbulence activity number ($\varepsilon/\nu N^2$). The black dots represent binned median values, while the error bars signify the standard error for the current data set. The solid black line is the least squares power law fit to the current data set (see text for details). Also shown for comparison are the power law fits from the field observations of *Davis and Monismith* [2011] (solid light gray line and light gray dots), the DNS simulations of *Shih et al.* [2005] (dashed light gray line), and the compiled laboratory data in *Barry* [2002] (dotted light gray line).

last two decades suggest that the mixing efficiency is not a universal constant. Indeed, there is a clear consensus that the mixing efficiency is highly variable (i.e., not constant) and depends on various parameters including the age of the turbulent patch, the origin of the turbulence, the strength of the stratification, the turbulence activity number, the location in the domain, etc. [e.g., *Rohr et al.*, 1984; *Itsweire et al.*, 1986; *Ivey and Imberger*, 1991, and the references therein; *Barry et al.*, 2001; *Barry*, 2002; *Smyth et al.*, 2001; *Peltier and Caulfield*, 2003; *Rehmann*, 2004; *Rehmann and Koseff*, 2004; *Shih et al.*, 2005; *Ivey et al.*, 2008, and the references therein, *Stretch et al.*, 2010; *Hult et al.*, 2011a, b; *Dunckley et al.*, 2012; *Lozovatsky and Fernando*, 2012; *Bluteau et al.*, 2013; *Bouffard and Boegman*, 2013]. More recently, field measurements of the flux Richardson number confirm a strong dependence on the turbulence activity number [*Davis and Monismith*, 2011; *Lozovatsky and Fernando*, 2012; *Bluteau et al.*, 2013; *Bouffard and Boegman*, 2013], in accordance with previous DNS results [e.g., *Shih et al.*, 2005]. Indeed, estimates of turbulent diffusivities are extremely sensitive to the choice of mixing efficiency used [cf. *Dunckley et al.*, 2012]. Figure 11c highlights the turbulent diffusivity calculated using the measured mixing efficiency (equation (10)). This is contrasted with Figure 11d, where the diffusivity is calculated from an assumed $\Gamma = 0.2$. There are substantial differences in the estimated diffusivities. Notably, the constant mixing efficiency formulation leads to overestimates of several orders of magnitude compared to the values calculated using the directly measured mixing efficiency.

The turbulence activity number is a common measure for characterizing turbulence in stratified environments, and several studies have noted the dependence of the flux Richardson number on the activity number [e.g., *Barry et al.*, 2001; *Barry*, 2002, and the references therein; *Shih et al.*, 2005, and the references therein; *Davis and Monismith*, 2011; *Lozovatsky and Fernando*, 2012; *Bluteau et al.*, 2013; *Bouffard and Boegman*, 2013]. The DNS simulations of *Shih et al.* [2005] show that in the intermediate range ($7 < \varepsilon/\nu N^2 < 100$), the constant flux Richardson number formulation ($R_f = 0.17$, $\Gamma = 0.2$) is valid; however, as the turbulence transitions into the energetic regime ($\varepsilon/\nu N^2 > 100$), the flux Richardson number displays a power law dependence on the activity number, $R_f \sim (\varepsilon/\nu N^2)^{-1/2}$. A power law dependence on the activity number was also found in the field observations of *Davis and Monismith* [2011], *Lozovatsky and Fernando* [2012], *Bluteau et al.* [2013], and *Bouffard and Boegman* [2013].

Figure 12 displays the flux Richardson number as a function of the turbulence activity number for the current data set, as well as the least squares power law fit to the data [i.e., $R_f \sim (\varepsilon/\nu N^2)^{-1/2}$]. The power law fit is much closer to the DNS measurements of *Shih et al.* [2005], compared to the field measurements of *Davis and Monismith* [2011]. This may be due to the fact that *Davis and Monismith* [2011] were inferring density fluxes from temperature fluctuations and salinity, the latter of which was determined from an empirical relationship between temperature and salinity. *Barry* [2002] compiled data from six laboratory studies [see *Barry*, 2002, and the references therein]) and suggested a best fit of, $R_f \sim 1/\left[1+0.4(\varepsilon/\nu N^2)^{2/3}\right]$ [see, e.g.,

Bluteau et al., 2013, equation (4)]. This power law fit (Figure 12) slightly underpredicts the mixing efficiency at a given activity number compared to the field observations in this study, but still suggests that R_f should decrease with increasing activity number. Finally, *Lozovatsky and Fernando* [2012] used observations from the stratified atmospheric boundary layer to derive a power law fit of $R_f \sim 50(\varepsilon/\nu N^2)^{-1/2}$, suggesting that the trend of decreasing mixing efficiency is shifted toward higher activity numbers (not shown). Nonetheless, the observations from this experiment (MOTOWN) confirm the general trend that for increasing turbulence activity numbers, the flux Richardson number decreases and approaches values much less than the constant value of 0.17 ($\Gamma = 0.2$). We note that the current observations reach turbulence activity numbers several orders of magnitude larger than previous DNS results and oceanic field observations [*Shih et al*., 2005; *Davis and Monismith*, 2011; *Bluteau et al*., 2013], which is of particular importance for oceanic field observations in energetic and highly turbulent environments. This particular parameterization is attractive for field-based oceanic observations since the turbulence activity number is composed of variables readily measured using vertical profiling instruments.

Several studies have examined the dependence of the flux Richardson number on other parameters such as the gradient Richardson number, $Ri = N^2/S^2$ [*Rohr et al*., 1984; *Holt et al*., 1992; *Rehmann and Koseff*, 2004; *Stretch et al*., 2010; *Davis and Monismith*, 2011], with variable outcomes. The current data set indicates that R_f increases for increasing Ri, but with considerable scatter [*Walter*, 2014, Appendix B]. The turbulence activity number can also be cast in terms of other nondimensional parameters, $\varepsilon/\nu N^2 \sim Re_t/Ri \sim Re_t Fr_t^2$, making other parameterizations of R_f possible (see discussion in *Shih et al*. [2005], *Bluteau et al*. [2013], *Mater and Venayagamoorthy* [2014], and *Walter* [2014, Appendix B]). Moreover, the atmospheric boundary layer field observations of *Lozovatsky and Fernando* [2012] do not support the idea of an unambiguous description of mixing efficiency as a function the activity number, given the disparity between their observations and DNS results/oceanic field observations. Furthermore, *Mater and Venayagamoorthy* [2014] suggest a multiparameter description of the mixing efficiency. This is the subject on ongoing work and will be reported elsewhere. We do note, however, that what is evident from this work, and the other studies discussed here, is that the mixing efficiency is highly variable (i.e., not constant) and strongly dependent on the turbulence activity number. Likewise, future oceanic observations and models need to adopt a variable mixing efficiency to accurately capture and quantify diapycnal mixing.

5. Summary and Implications

We collected high-frequency measurements of stratified turbulence throughout the water column in the nearshore environment of Monterey Bay, CA, using a cabled observatory system and an underwater turbulence flux tower. The measurements collected offer a unique look into the dynamics of stratified turbulence in the coastal environment for several reasons: (1) nearly 2 weeks of continuous measurements of collocated velocity and density fluctuations at 64 Hz were collected allowing direct estimates of momentum and density fluxes, as well as mixing efficiencies; (2) the observations are not confined to the near-bed region, similar to previous studies, but they extend into the stratified interior providing insight into the vertical evolution of the stratified turbulence and mixing dynamics in various stratified turbulence regimes; and (3) the measurements captured transient stratification and mixing events associated with nearshore internal bores, thus providing a unique look into the evolution of stratified turbulence in the presence of nearshore internal bores with high spatial and temporal coverage.

Measurements at the tower location confirm previous observations of nonlinear internal bores that drive intrusions of dense, offshore waters [e.g., *Walter et al*., 2012, 2014]. We show that individual bores can drive substantial changes to local turbulence and mixing dynamics, with considerable differences between the leading and trailing edges of the bores. The trailing edge of the bore is characterized by elevated TKE dissipation and shear production values by almost an order of magnitude compared to the leading edge; however, lower mixing efficiencies lead to measured turbulent diffusivities that are not as large as expected under the assumption of a constant mixing efficiency, but that are still higher than the leading edge. These aspects are likely due to a combination of the "non-canonical" structure of the bore and the local internal Iribarren number [cf. *Walter et al*., 2012], as well as the mixing efficiency dependence on various parameters such as the turbulence activity number.

Finally, we present direct measurements of the flux Richardson number, and hence the mixing efficiency, over a variety of forcing regimes. Our results suggest that the most efficient mixing occurs in regions of

buoyancy-controlled turbulence ($Fr_t < 1$), consistent with previous field observations [*Davis and Monismith*, 2011; *Dunckley et al*., 2012]. Notably, this work adds to a growing body of the literature that suggests the mixing efficiency is not a universal constant (see the recent review by *Ivey et al*. [2008] and the references therein). Specifically, the findings also confirm, and extend, previous DNS [*Shih et al*., 2005], laboratory [*Barry et al*., 2001; *Barry*, 2002, and the references therein], and field [*Davis and Monismith*, 2011; *Lozovatsky and Fernando*, 2012; *Bluteau et al*., 2013; *Bouffard and Boegman*, 2013] parameterizations of the flux Richardson number, and hence the mixing efficiency, as a function of the turbulence activity number and confirm a power law dependence on the activity number. We also found that the widely used assumption of a constant mixing efficiency, $\Gamma = 0.2$, leads to significant overestimates of the vertical turbulent diffusivity compared to values calculated using the directly measured mixing efficiency in the current data set, with important implications for both regional and local mixing processes such as heat and energy budgets, larval connectivity, nutrient cycling, hypoxia development, and primary production [e.g., *Wolanski and Pickard*, 1983; *Leichter et al*., 1996; *Chan et al*., 2008].

It is clear that the turbulence structure in the presence of nearshore internal bores is substantially different than that expected from the traditional model of a bottom mixed layer under a stratified interior. The elevated levels of turbulent mixing within the stratified interior are an important source of mixing that affect many physical and biological processes. Currently, large-scale models, such as the Regional Ocean Modeling System (ROMS), along the CCLME do not accurately capture the physics of nearshore internal bores. It is critical that fine-scale mixing and transport due to shoaling internal waves and bores in the nearshore coastal environment be better resolved (with careful consideration of the nonhydrostatic nature of these features), or accurately parameterized, to avoid errors in assessing nearshore dynamics. Furthermore, internal bores are a mechanism by which deeper, offshore Pacific waters with low dissolved oxygen (DO) and pH levels [e.g., *Checkley and Barth*, 2009] are supplied to the nearshore [*Walter et al*., 2012, 2014]. Understanding how the mixing evolves throughout the stratified interior is crucial to assessing nearshore DO/pH variability, the potential development of hypoxia, and ocean acidification in this region [e.g., *Booth et al*., 2012]. Indeed, we surmise that the strength and intensity of nearshore bores, and in particular the trailing edge of the bore, may be important factors governing water column DO and pH levels in this region [see *Walter et al*., 2014, for results and discussion of oxygen variability during this experiment].

Acknowledgments

This work was funded by the National Science Foundation through grant OCE-1235552. R. Walter received support from the Stanford Graduate Fellowship. We thank the members of the Environmental Fluid Mechanics Laboratory and Paul Leary for dive support and help in the field. We acknowledge helpful discussions with Robert Arthur, Jamie Dunckley, and Oliver Fringer. This manuscript benefited from the helpful comments of two anonymous reviewers. Data used in this study are available by contacting R. Walter. Bathymetry data used in this study were acquired, processed, archived, and distributed by the Seafloor Mapping Lab of California State University Monterey Bay.

References

Arthur, R. S., and O. B. Fringer (2014), The dynamics of breaking internal solitary waves on slopes, *J. Fluid. Mech.*, *761*, 360–398.

Barry, M. E. (2002), Mixing in stratified turbulence, PhD thesis, University of Western Australia, Centre for Water Research.

Barry, M. E., G. N. Ivey, K. B. Winters, and J. Imberger (2001), Measurements of diapycnal diffusivities in stratified fluids, *J. Fluid Mech.*, *442*, 267–291.

Becherer, J. K., and L. Umlauf (2011), Boundary mixing in lakes. 1: Modeling the effect of shear-induced convection, *J. Geophys. Res.*, *116*, C10017, doi:10.1029/2011JC007119.

Bluteau, C. E., N. L. Jones, and G. N. Ivey (2011), Estimating turbulent kinetic energy dissipation using the inertial subrange method in environmental flows, *Limnol. Oceanogr. Methods*, *9*, 302–321.

Bluteau, C. E., N. L. Jones, and G. N. Ivey (2013), Turbulent mixing efficiency at an energetic ocean site, *J. Geophys. Res. Oceans*, *118*, 4662–4672, doi:10.1002/jgrc.20292.

Boehm, A. B., B. F. Sanders, and C. D. Winant (2002), Cross-shelf transport at Huntington Beach. Implications for the fate of sewage discharged through an offshore ocean outfall, *Environ. Sci. Technol.*, *36*, 1899–1906.

Booth, J. A. T., E. E. McPhee-Shaw, P. Chua, E. Kingsley, M. Denny, R. Phillips, S. J. Bograd, L. D. Zeidberg, and W. F. Gilly (2012), Natural intrusions of hypoxic, low pH water into nearshore marine environments on the California coast, *Cont. Shelf Res.*, *45*, 108–115.

Bouffard, D., and L. Boegman (2013), A diapycnal diffusivity model for stratified environmental flows, *Dyn. Atmos. Oceans*, *61–62*, 14–34.

Breaker, L. C., and W. W. Broenkow (1994), The circulation of Monterey Bay and related processes, *Oceanogr. Mar. Biol.*, *32*, 1–64.

Bricker, J. D., and S. G. Monismith (2007), Spectral wave-turbulence decomposition, *J. Atmos. Oceanic Technol.*, *24*, 1479–1487.

Carter, G. S. (2010), Barotropic and baroclinic M_2 tides in the Monterey Bay region, *J. Phys. Oceanogr.*, *40*, 1766–1783.

Carter, G. S., M. C. Gregg, and R. Lien (2005), Internal waves, solitary-like waves, and mixing on the Monterey Bay shelf, *Cont. Shelf Res.*, *25*, 1499–1520.

Chan, F., J. A. Barth, J. Lubchenco, A. Kirincich, H. Weeks, W. T. Peterson, and B. A. Menge (2008), Emergence of anoxia in the California Current large marine ecosystem, *Science*, *319*, 920–920.

Checkley, D. M., Jr., and J. A. Barth (2009), Patterns and processes in the California Current System, *Prog. Oceanogr.*, *83*, 49–64.

Davis, K. A., and S. G. Monismith (2011), The modification of bottom boundary layer turbulence and mixing by internal waves shoaling on a barrier reef, *J. Phys. Oceanogr.*, *41*, 2223–2241.

Dunckley, J. F., J. R. Koseff, J. V. Steinbuck, S. G. Monismith, and A. Genin (2012), Comparison of mixing efficiency and vertical diffusivity models from temperature microstructure, *J. Geophys. Res.*, *117*, C10008, doi:10.1029/2012JC007967.

Emery, W. J., and R. E. Thomson (2004), *Data Analysis Methods in Physical Oceanography*, 2nd and revised ed., 638 pp., Elsevier, Amsterdam.

Feddersen, F., and A. J. Williams (2007), Direct estimation of the Reynolds stress vertical structure in the nearshore, *J. Atmos. Oceanic Technol.*, *24*, 102–116.

Feddersen, F., J. H. Trowbridge, and A. J. Williams (2007), Vertical structure of dissipation in the nearshore, *J. Phys. Oceanogr.*, *37*, 1764–1777.
Gargett, A. E., T. R. Osborn, and P. W. Nasmyth (1984), Local isotropy and the decay of turbulence in a stratified fluid, *J. Fluid Mech.*, *144*, 231–280.
Gerbi, G. P., J. H. Trowbridge, J. B. Edson, A. J. Plueddemann, E. A. Terray, and J. J. Fredericks (2008), Measurements of momentum and heat flux across the air-sea interface, *J. Phys. Oceanogr.*, *38*, 1054–1072.
Goring, D. G., and V. I. Nikora (2002), Despiking acoustic Doppler velocimeter data, *J. Hydraul. Eng.*, *128*(1), 117–126.
Gregg, M. C. (1989), Scaling turbulent dissipation in the thermocline, *J. Geophys. Res.*, *94*, 9686–9698.
Gross, T. F., and A. R. M. Nowell (1983), Mean flow and turbulence scaling in a tidal boundary layer, *Cont. Shelf Res.*, *2*, 109–126, doi: 10.1016/0278-4343(83)90011-0.
Hansen, J. C. R., and M. A. Reidenbach (2012), Wave and tidally driven flows in eelgrass beds and their effect on sediment suspension, *Mar. Ecol. Prog. Ser.*, *448*, 271–287.
Holt, S. E., J. R. Koseff, and J. H. Ferziger (1992), A numerical study of the evolution and structure of homogeneous stably stratified sheared turbulence, *J. Fluid Mech.*, *237*, 499–539.
Hult, E. L., C. D. Troy, and J. R. Koseff (2011a), The mixing efficiency of interfacial waves breaking at a ridge. 1: Overall mixing efficiency, *J. Geophys. Res.*, *116*, C02003, doi:10.1029/2010JC006488.
Hult, E. L., C. D. Troy, and J. R. Koseff (2011b), The mixing efficiency of interfacial waves breaking at a ridge. 2: Local mixing processes, *J. Geophys. Res.*, *116*, C02004, doi:10.1029/2010JC006488.
Itsweire, E. C., K. N. Helland, and C. W. Van Atta (1986), The evolution of grid-generated turbulence in a stably stratified fluid, *J. Fluid Mech.*, *162*, 299–338.
Ivey, G. N., and J. Imberger (1991), On the nature of turbulence in a stratified fluid. Part I: The energetics of mixing, *J. Phys. Oceanogr.*, *21*, 650–658.
Ivey, G. N., K. B. Winters, and J. R. Koseff (2008), Density stratification, turbulence, but how much mixing?, *Annu. Rev. Fluid Mech.*, *40*, 168–184.
Kaimal, J. C., J. C. Wyngaard, Y. Izumi, and O. R. Coté (1972), Spectral characteristics of surface-layer turbulence, *Q. J. R. Meteorol. Soc.*, *98*, 563–589.
Kunze, E., L. K. Rosenfeld, G. S. Carter, and M. C. Gregg (2002), Internal waves in Monterey Submarine Canyon, *J. Phys. Oceanogr.*, *32*, 1890–1913.
Leichter, J. J., S. R. Wing, S. L. Miller, and M. W. Denny (1996), Pulsed delivery of subthermocline water to Conch Reef (Florida Keys) by internal tidal bores, *Limnol. Oceanogr.*, *41*, 1490–1501.
Lorrai, C., L. Umlauf, J. K. Becherer, A. Lorke, and A. Wüest (2011), Boundary mixing in lakes. 2: Combined effects of shear- and convectively induced turbulence on basin-scale mixing, *J. Geophys. Res.*, *116*, C10018, doi:10.1029/2011JC007121.
Lozovatsky, I. D., and H. J. S. Fernando (2012), Mixing efficiency in natural flows, *Philos. Trans. R. Soc. A*, *371*, 20120213, doi:10.1098/rsta.2012.0213.
Luketina, D. A., and J. Imberger (1987), Characteristics of a surface buoyant jet, *J. Geophys. Res.*, *92*, 5435–5447, doi:10.1029/JC092iC05p05435.
Lumley, J. L., and E. A. Terray (1983), Kinematics of turbulence convected by a random wave field, *J. Phys. Oceanogr.*, *13*, 2000–2007.
MacVean, L. J., and J. R. Lacy (2014), Interactions between waves, sediment, and turbulence on a shallow estuarine mudflat, *J. Geophys. Res. Oceans*, *119*, 1534–1553, doi:10.1002/2013JC009477.
Mater, B. D., and S. K. Venayagamoorthy (2014), The quest for an unambiguous parameterization of mixing efficiency in stably stratified geophysical flows, *Geophys. Res. Lett.*, *41*, 4646–4653, doi:10.1002/2014GL060571.
Moum, J. N., and T. P. Rippeth (2009), Do observations adequately resolve the natural variability of oceanic turbulence?, *J. Mar. Syst.*, *77*, 409–417.
Moum, J. N., D. M. Farmer, W. D. Smyth, L. Armi, and S. Vagle (2003), Structure and generation of turbulence at interfaces strained by internal solitary waves propagating shoreward over the continental shelf, *J. Phys. Oceanogr.*, *33*, 2093–2112.
Munk, W., and C. Wunsch (1998), Abyssal recipes. II: Energetics of tidal and wind mixing, *Deep Sea Res., Part A*, *45*, 1977–2010.
Osborn, T. R. (1980), Estimates of the local rate of vertical diffusion from dissipation measurements, *J. Phys. Oceanogr.*, *10*, 83–89.
Peltier, W. R., and C. P. Caulfield (2003), Mixing efficiency in stratified shear flows, *Annu. Rev. Fluid Mech.*, *35*, 135–167, doi:10.1146/annurev.fluid.35.101101.161144.
Perlin, A., J. N. Moum, J. M. Klymak, M. D. Levine, T. Boyd, and P. M. Kosro (2005), A modified law-of-the-wall applied to oceanic bottom boundary layers, *J. Geophys. Res.*, *110*, C10S10, doi:10.1029/2004JC002310.
Petruncio, E. T., L. K. Rosenfeld, and J. D. Paduan (1998), Observations of the internal tide in Monterey Canyon, *J. Phys. Oceanogr.*, *28*, 1873–1903.
Pineda, J. (1994), Internal tidal bores in the nearshore: Warm-water fronts, seaward gravity currents and the onshore transport of neustonic larvae, *J. Mar. Res.*, *52*, 427–458.
Pope, S. B. (2000), *Turbulent Flows*, 771 pp., Cambridge Univ. Press, Cambridge, U. K.
Rehmann, C. R. (2004), Scaling for the mixing efficiency of stratified grid turbulence, *J. Hydraul. Res.*, *42*(1), 35–42.
Rehmann, C. R., and J. R. Koseff (2004), Mean potential energy change in stratified grid turbulence, *Dyn. Atmos. Oceans*, *37*, 271–294.
Reidenbach, M. A., S. G. Monismith, J. R. Koseff, G. Yahel, and A. Genin (2006), Boundary layer turbulence and flow structure over a fringing coral reef, *Limnol. Oceanogr. Methods*, *51*, 1956–1968.
Rohr, J. J., E. C. Itsweire, and C. W. Van Atta (1984), Mixing efficiency in stably-stratified decaying turbulence, *Geophys. Astrophys. Fluid Dyn.*, *29*(1–4), 221–236.
Rosenfeld, L. K., I. Shulman, M. Cook, J. D. Paduan, and L. Shulman (2009), Methodology for regional tidal model evaluation, with application to Central California, *Deep Sea Res., Part II*, *56*, 199–218.
Sanford, T. B., and R. Lien (1999), Turbulent properties in a homogeneous tidal bottom boundary layer, *J. Geophys. Res.*, *104*, 1245–1257.
Shaw, W. J., and J. H. Trowbridge (2001), The direct estimation of near-bottom fluxes in the presence of energetic wave motions, *J. Atmos. Oceanic Technol.*, *18*, 1540–1557.
Shaw, W. J., J. H. Trowbridge, and A. J. Williams III (2001), Budgets of turbulent kinetic energy and scalar variance in the continental shelf bottom boundary layer, *J. Geophys. Res.*, *106*, 9551–9564.
Shih, L. H., J. R. Koseff, G. N. Ivey, and J. H. Ferziger (2005), Parameterization of turbulent fluxes and scales using homogeneous sheared stably stratified turbulence simulations, *J. Fluid Mech.*, *525*, 193.

Smyth, W. D., J. N. Moum, and D. R. Caldwell (2001), The efficiency of mixing in turbulent patches: Inferences from direct simulations and microstructure observations, *J. Phys. Oceanogr.*, *31*, 1969–1992.
Soulsby, R. L. (1980), Selecting record length and digitization rate for near-bed turbulence measurements, *J. Phys. Oceanogr.*, *10*, 208–219.
Stretch, D. D., J. W. Rottman, S. K. Venayagamoorthy, K. K. Nomura, and C. R. Rehmann (2010), Mixing efficiency in decaying stably stratified turbulence, *Dyn. Atmos. Oceans*, *49*, 25–36.
Tennekes, H., and J. L. Lumley (1972), *A First Course in Turbulence*, MIT Press, Cambridge, Mass.
Trowbridge, J. H. (1998), On a technique for measurement of turbulent shear stress in the presence of surface waves, *J. Atmos. Oceanic Technol.*, *15*, 290–298.
Trowbridge, J. H., W. R. Geyer, M. M. Bowen, and A. J. Williams (1999), Near-bottom turbulence measurements in a partially mixed estuary: Turbulent energy balance, velocity structure, and along-channel momentum balance, *J. Phys. Oceanogr.*, *29*, 3056–3072.
Voulgaris, G., and J. H. Trowbridge (1998), Evaluation of the acoustic Doppler velocimeter (ADV) for turbulence measurements, *J. Atmos. Oceanic Technol.*, *15*, 272–289.
Walter, R. K. (2014), Nonlinear internal waves, internal bores, and turbulent mixing in the nearshore coastal environment, PhD dissertation, Dep. of Civ. and Environ. Eng., Stanford Univ., Stanford, Calif.
Walter, R. K., N. J. Nidieko, and S. G. Monismith (2011), Similarity scaling of turbulence spectra and cospectra in a shallow tidal flow, *J. Geophys. Res.*, *116*, C10019, doi:10.1029/2011JC007144.
Walter, R. K., C. B. Woodson, R. S. Arthur, O. B. Fringer, and S. G. Monismith (2012), Nearshore internal bores and turbulent mixing in southern Monterey Bay, *J. Geophys. Res.*, *177*, C07017, doi:10.1029/2012JC008115.
Walter, R. K., C. B. Woodson, P. R. Leary, and S. G. Monismith (2014), Connecting wind-driven upwelling and offshore stratification to nearshore internal bores and oxygen variability, *J. Geophys. Res. Oceans*, *119*, 3517–3534, doi:10.1002/2014JC009998.
Waterhouse, A. F., et al. (2014), Global patterns of diapycnal mixing from measurements of the turbulent dissipation rate, *J. Phys. Oceanogr.*, *44*, 1854–1872.
Wilson, M. L., D. R. Webster, and M. J. Weissburg (2013), Spatial and temporal variation in the hydrodynamic landscape in intertidal salt marsh systems, *Limnol. Oceanogr. Fluids Environ.*, *3*, 156–172.
Wolanski, E., and G. Pickard (1983), Upwelling by internal tides and Kelvin waves at the continental shelf break on the Great Barrier Reef, *Mar. Freshwater Res.*, *34*, 65–80.
Woodson, C. B., L. Washburn, J. A. Barth, D. J. Hoover, A. R. Kirincich, M. A. McManus, J. P. Ryan, and J. Tyburczy (2009), Northern Monterey Bay upwelling shadow front: Observations of a coastally and surface-trapped buoyant plume, *J. Geophys. Res.*, *114*, C12013, doi:10.1029/2009JC005623.
Woodson, C. B., et al. (2011), Observations of internal wave packets propagating along-shelf in northern Monterey Bay, *Geophys. Res. Lett.*, *38*, L01605, doi:10.1029/2010GL045453.